Tectonic structure, lithology, and hydrothermal signature of the Rainbow massif (Mid-Atlantic Ridge 36°14'N)

Muriel Andreani, Javier Escartin, Adélie Delacour, Benoit Ildefonse, Marguerite Godard, Jerome Dyment, Anthony E. Fallick, Yves Fouquet

AGU PUBLICATIONS

Geochemistry, Geophysics, Geosystems

RESEARCH ARTICLE
10.1002/2014GC005269

Special Section:
Oceanic detachment faults

Tectonic structure, lithology, and hydrothermal signature of the Rainbow massif (Mid-Atlantic Ridge 36°14′N)

Muriel Andreani[1], Javier Escartin[2], Adélie Delacour[3], Benoit Ildefonse[4], Marguerite Godard[4], Jérôme Dyment[2], Anthony E. Fallick[5], and Yves Fouquet[6]

[1]Laboratoire de Géologie de Lyon, UMR 5672, ENS, Université Lyon 1, Lyon, France, [2]Institut de Physique du Globe de Paris, CNRS UMR 7154, Paris, France, [3]Laboratoire Magmas et Volcans, CNRS UMR 6524, Université Jean Monnet, Saint-Etienne, France, [4]Géosciences Montpellier, CNRS UMR 5243, Université Montpellier 2, Montpellier, France, [5]Scottish Universities Environmental Research Centre, Glasgow, UK, [6]IFREMER, Centre de Brest, Plouzane, France

Key Points:
- Rainbow massif uplifted by now inactive west dipping detachment
- Oblique faults dissect the massif and localize hydrothermalism for last 100 kyr
- Petrography and geochemistry unravel high and low-T fluid-rock reaction history

Supporting Information:
- Readme
- Tables S1–S4
- Figure S1
- Supplementary Material

Correspondence to:
M. Andreani,
muriel.andreani@univ-lyon1.fr

Citation:
Andreani, M., J. Escartin, A. Delacour, B. Ildefonse, M. Godard, J. Dyment, A. E. Fallick, and Y. Fouquet (2014), Tectonic structure, lithology, and hydrothermal signature of the Rainbow massif (Mid-Atlantic Ridge 36°14′N), *Geochem. Geophys. Geosyst.*, *15*, 3543–3571, doi:10.1002/2014GC005269.

Received 28 JAN 2014
Accepted 9 JUL 2014
Accepted article online 12 JUL 2014
Published online 8 SEP 2014

Abstract Rainbow is a dome-shaped massif at the 36°14′N nontransform offset along the Mid-Atlantic Ridge. It hosts three ultramafic-hosted hydrothermal sites: Rainbow is active and high temperature; Clamstone and Ghost City are fossil and low temperature. The MoMARDREAM cruises (2007, 2008) presented here provided extensive rock sampling throughout the massif that constrains the geological setting of hydrothermal activity. The lithology is heterogeneous with abundant serpentinites surrounding gabbros, troctolites, chromitites, plagiogranites, and basalts. We propose that a W dipping detachment fault, now inactive, uplifted the massif and exhumed these deep-seated rocks. Present-day deformation is accommodated by SSW-NNE faults and fissures, consistent with oblique teleseismic focal mechanisms and stress rotation across the discontinuity. Faults localize fluid flow and control the location of fossil and active hydrothermal fields that appear to be ephemeral and lacking in spatiotemporal progression. Markers of high-temperature hydrothermal activity (~350°C) are restricted to some samples from the active field while a more diffuse, lower temperature hydrothermal activity (<220°C) is inferred at various locations through anomalously high As, Sb, and Pb contents, attributed to element incorporation in serpentines or microscale-sulfide precipitation. Petrographic and geochemical analyses show that the dominant basement alteration is pervasive peridotite serpentinization at ~160–260°C, attributed to fluids chemically similar to those venting at Rainbow, and controlled by concomitant alteration of mafic-ultramafic units at depth. Rainbow provides a model for fluid circulation, possibly applicable to hydrothermalism at oceanic detachments elsewhere, where both low-temperature serpentinization and magmatic-driven high-temperature outflow develop contemporaneously, channeled by faults in the footwall and not along the detachment fault.

1. Introduction

The high-temperature (high-T) Rainbow hydrothermal field is located on the western flank of the Rainbow massif at 36°14′N along the Mid-Atlantic Ridge (MAR). The composition of venting fluids records seawater interaction with an ultramafic substrate [*German et al.*, 1996; *Charlou et al.*, 1997; *Fouquet et al.*, 1997]. Two additional low-temperature (low-T), fossil hydrothermal sites, Ghost City and Clamstone, were found ~1–2 km NE and E of Rainbow field, respectively [*Lartaud et al.*, 2010, 2011]. The first ultramafic-hosted hydrothermal site to be discovered was Logatchev, located at 14°45′N on the MAR [*Bogdanov et al.*, 1995]. Since then, several inactive and active ultramafic-hosted sites have been identified along the MAR, including Menez Hom at 37°9′N, Saldanha at 36°34′N, Lost City at 30°N, Semyonov at 13°30′N, Ashadze at 12°58′N, and Nibelungen at 8.3°S [e.g., *Barriga et al.*, 1998; *Beltenev et al.*, 2007; *Fouquet et al.*, 2010; *Kelley et al.*, 2001; *Melchert et al.*, 2008; *Ondréas et al.*, 2012]. Active and inactive sites, some also likely hosted on an ultramafic basement, have been reported along the South-West Indian Ridge (SWIR) [e.g., *German et al.*, 1998; *Bach et al.*, 2002], the Mid-Cayman ridge [*German et al.*, 2010a], the Central Indian Ridge [*Kumagai et al.*, 2008], and the Arctic Ridges [*Pedersen et al.*, 2010]. A site has also been found in a fore-arc setting in the Mariana Trench, but with no evidence of active fluid venting (Shinkai Seep Field, 11°39′N–143°02′E) [*Ohara et al.*, 2012].

Three types of ultramafic-hosted hydrothermal sites can be distinguished based on their fluid characteristics: (1) high-T hydrothermal sites with high-T (350–365°C) and low pH (<4) focused fluid flow venting from

metal-rich sulfide chimneys, such as Rainbow, Logatchev, and Ashadze [*Charlou et al*., 2010]; (2) medium-T hydrothermal sites with high pH (>9), less focused fluid flow venting from carbonate chimneys at T up to 90°C, such as the Lost City field located 15 km off axis and on ~1.5 Myr old terrains [*Kelley et al*., 2001, 2005; *Grimes et al*., 2008]; and (3) low-T hydrothermal sites with diffuse and pervasive seepages, at apparently low temperatures T (<30°C), and of unknown pH, such as Saldhana and Menez Hom [*Barriga et al*., 1998]. However, all vent fluids are strongly enriched in hydrogen (10–26 mM) and methane (1–3 mM) [*Charlou et al*., 2002, 2010; *Douville et al*., 2002; *Melchert et al*., 2008; *Fouquet et al*., 2010], compared with their basalt-hosted analogues.

The increasing evidence that ultramafic-hosted hydrothermal sites are common and abundant suggests that mantle-seawater interactions contribute significantly to global chemical and heat exchanges between the ocean and the lithosphere. These sites require active tectonic processes to exhume mantle rocks and sustain fluid circulation. Numerous ultramafic-hosted hydrothermal sites are found in association with oceanic core complexes [e.g., *Escartín et al*., 2008] where long-lived detachment faults are pathways for fluid flow, leading to the establishment of focused high-T to low-T vents with increasing distance from the ridge axis [e.g., *deMartin et al*., 2007; *Fouquet et al*., 2010; *McCaig et al*., 2010]. Fluid circulation can be maintained for several million years off axis through fractured detachment footwall [*Hirose and Hayman*, 2008; *Tucholke et al*., 2013].

While the chemistry of Rainbow fluids and associated hydrothermal deposits has been extensively studied [*Charlou et al*., 2002; *Douville et al*., 2002; *Konn et al*., 2009; *Seyfried et al*., 2011], the structure, lithology, and geodynamic origin of the Rainbow massif, which provide the setting for past and present hydrothermal activity, are poorly constrained. Prior cruises (FLORES 1997, IRIS 2001, SEAHMA 2002) [*Barriga et al*., 1997; *Fouquet et al*., 1998; *Fouquet and IRIS Scientific Party*, 2001; *Barriga et al*., 2003] focused on studying the hydrothermally active area where ultramafic rocks and hydrothermal deposits have been sampled (Figure 1), indicating sulfide mineralization of a mafic nature that overprints the serpentinization of the peridotites [*Marques et al*., 2007]. Together with fluid temperature and heat flux, this supports the contribution of an intrusive magmatic unit to sustain present-day hydrothermalism [*Douville et al*., 2002; *Marques et al*., 2007; *Allen and Seyfried*, 2004; *German et al*., 1996, 2010b]. Furthermore, the fluids seem to be influenced by a magnetite-chlorite-talc buffer [*Seyfried et al*., 2011], more representative of the hydration of olivine-rich gabbroic intrusions than that of peridotite.

The geological setting and history of the massif is critical to understand the nature and the distribution of hydrothermal activity. A diapiric origin was originally proposed for this structure [*Fouquet et al*., 1998; *Charlou et al*., 2010]. Subsequently, *Gracia et al*. [1998, 2000] postulated a tectonic uplift associated with two low-angle normal faults along the East and West flanks of the Rainbow and similar nontransform offset (NTO) massifs in this area. The east dipping thin layer of old basalt described ~1 km east of the active area by *Fouquet et al*. [1998] was later interpreted by *McCaig et al*. [2010] as an indication of detachment breakaway close to the top of the massif, with the detachment fault dipping to the west.

The rock sampling around the high-T vent field was too limited to document the interplay between the tectonic evolution of the massif, the magmatic activity inferred from gabbroic intrusions, and the hydrothermal activity. We present here a synthesis and interpretation of prior and newly acquired geological and tectonic information at the massif scale. We also investigate the nature and conditions of hydrothermal circulation, as recorded by the sampled rocks. These results are used to propose a revised model for the formation and the tectonic framework of the Rainbow massif and to discuss the controls on the distribution and nature of hydrothermal activity.

2. Geological Setting

The dome-shaped Rainbow massif is located at the center of a right-stepping NTO (Figure 1a) that separates the AMAR and South AMAR ridge segments of the Northern MAR [*Gracia et al*., 2000]. This discontinuity is contiguous to other NTO that extend south of the Azores, bounding ridge segments [*Gracia et al*., 2000] and accounting for the overall oblique orientation of the ridge axis relative to spreading. The present-day full spreading rate of this MAR in this region is ~21.5 mm/yr [*Sloan and Patriat*, 1992; *Le Douaran et al*., 1982].

The Rainbow massif hosts active and fossil hydrothermal sites, spanning more than 100 kyr [*Kuznetsov et al*., 2006; *Lartaud et al*., 2010, 2011], and documented at three sites. The active Rainbow field, located on the western flank of the massif near its summit at 2300 m water depth (Figure 1), extends over a surface of

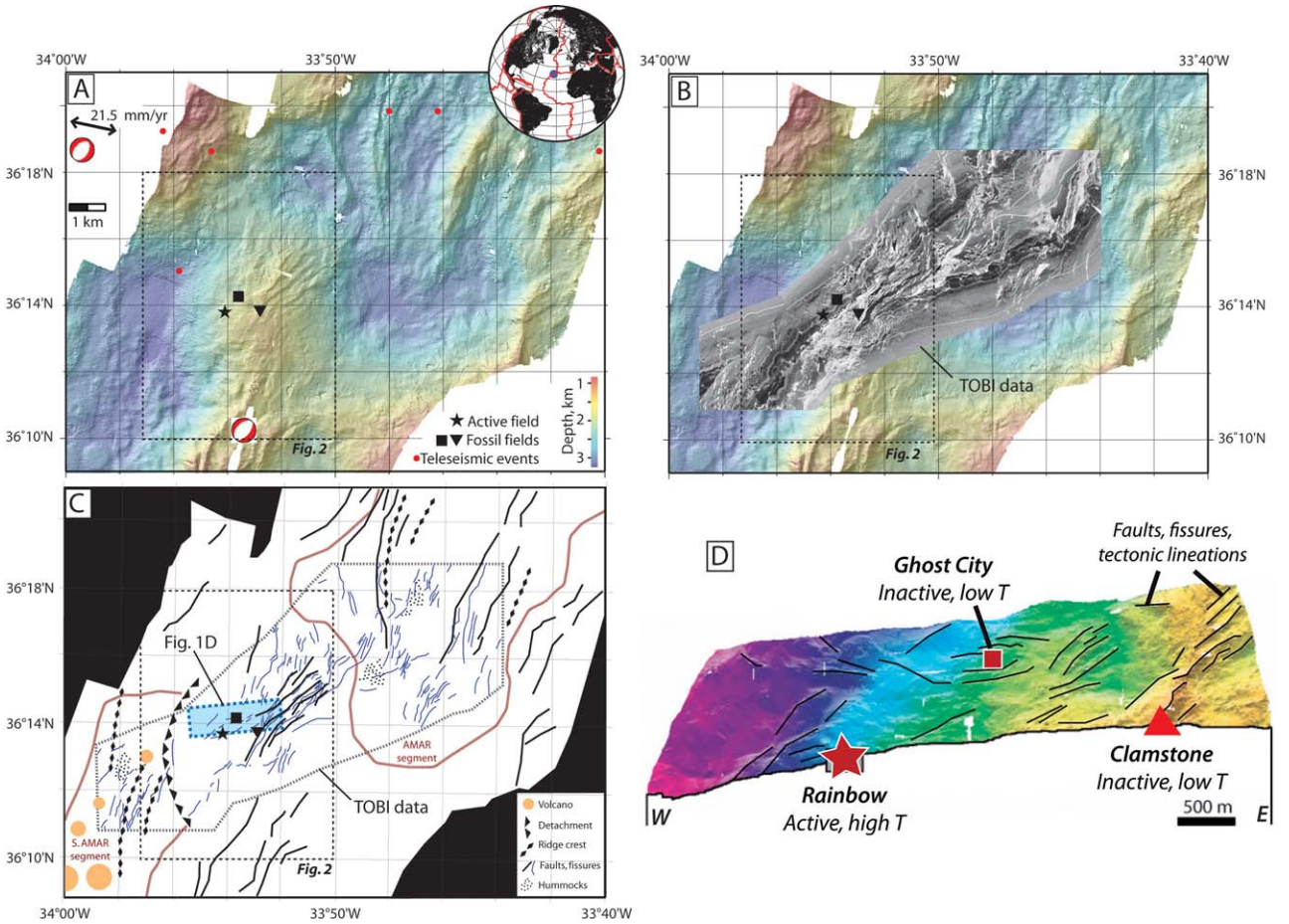

Figure 1. (a) Bathymetric map of the Rainbow massif area with the locations of active and ancient hydrothermal sites, and available teleseismic data. The star indicates the location of the active Rainbow hydrothermal field, while the square and triangle indicate the locations of the fossil Ghost City and Clamstone hydrothermal fields, respectively. (b) High-resolution TOBI side-scan sonar map from *Gracia et al.* [2000] superposed on the bathymetric map. (c) Interpretative structural scheme of the Rainbow massif area. The black dotted area indicates the position of TOBI data. (d) Microbathymetry of the massif area hosting the fossil and active hydrothermal sites [modified from *Lartaud et al.*, 2010].

$\sim$200 $\times$ 100 m. It is hosted in serpentinized peridotites that crop out around the active site [*Fouquet et al.*, 1997; *Barriga et al.*, 1997; *Marques et al.*, 2006; *Charlou et al.*, 2010]. This area is associated with a local positive magnetic anomaly [*Dyment et al.*, 2005; *Tivey and Dyment*, 2010], which may result from magnetite precipitation associated with serpentinization or from the presence of magnetic iron sulfide in sufficient quantities [*Tivey and Dyment*, 2010]. In contrast, basalt-hosted sites with high-T hydrothermal fluid circulation undergo demagnetization of the substrate and are associated with negative magnetic anomalies [*Tivey et al.*, 1993; *Tivey and Johnson*, 2002; *Tivey and Dyment*, 2010]. Sampled hydrothermal fluids are high-T ($>$300°C), acid (pH $\sim$2.8), and metal-rich with high chlorinity ($>$750 mM) [*Douville et al.*, 2002; *Seyfried et al.*, 2011]. They present the highest abundances in REE and transition metals (particularly in Fe, Mn, Cu, Zn, Co, and Ni) reported for a MAR hydrothermal vent field, including basalt-hosted systems [*Fouquet et al.*, 2010]. The hydrothermal deposits, which are Cu-Zn-Co-rich [*Marques et al.*, 2007], display ages suggesting active venting for the last 23 $\pm$ 1.5 kyr [*Kuznetsov et al.*, 2006], with no constraints on whether this activity has been continuous or discontinuous. Present-day flux estimates associated with this site yield water mass and heat fluxes of up to 450 L/s and 0.5 GW, respectively, together with important chemical fluxes (e.g., 10 and 1 mol/s for Fe and CH_4, respectively) [*German et al.*, 2010b]. Based on thermal arguments, this major heat flux requires heat mining from a large volume of axial crust, possibly extending several tens of kilometers along axis [*German et al.*, 2010b]. The location and the geometry of the heat source(s) are currently unknown.

Two fossil hydrothermal sites have been recently identified, in close proximity to the active Rainbow field (Figure 1). Ghost City, located 2 km NE of the Rainbow field, at a water depth of 2100 m, contains fossil

gastropods and chemosynthetic clams in carbonate sediments, which have been dated at 110 ± 0.9 kyr [*Lartaud et al*., 2011]. In contrast to the active Rainbow field, fossil fluids are inferred to have been metal-poor, and the site is associated with nearby peridotites and gabbros [*Lartaud et al*., 2011]. The second site, Clamstone, located 2.5 km E of Rainbow, at a water depth of ~1980 m, is associated with serpentinized peridotites dredged nearby. This site shows an abundant accumulation of shell-rich carbonates dated at 25 kyr, and the inferred nature of the hydrothermal fluids that percolated through the sediments associated with this site is similar to those from Ghost City [*Lartaud et al*., 2010]. These two sites display hydrothermal activity different in nature to that of the active Rainbow site, but very similar to that of Lost City [*Lartaud et al*., 2010, 2011], for which the hypothesis of the serpentinization reaction sustaining hydrothermal convection alone, with no magmatic heat supply, is still debated [*Lowell and Rona*, 2002; *Allen and Seyfried*, 2004; *Emmanuel and Berkowitz*, 2006].

3. Methods

In addition to shipboard bathymetry (Figure 1a), the Rainbow massif was surveyed with the high-resolution deep-towed TOBI side-scan sonar system (Figures 1b and 1c) during the 1994 HEAT cruise [*German et al*., 1996]. These data were used to constrain the geomorphology and tectonic framework of the Rainbow massif, on which the first exhaustive and comprehensive geological study was carried out during the MoMAR-DREAM oceanographic cruises in 2007 and 2008, onboard N/O Pourquoi Pas? and L'Atalante (IFREMER, France), respectively. In situ sampling and observations were performed with the deep-sea submersible Nautile and the remotely operated vehicle (ROV) Victor. Nautile conducted two geology-oriented dives during the 2007 cruise (M7-PL4 and M7-PL10 tracks in Figure 2). ROV Victor conducted four geology-oriented dives in 2008 that focused primarily on the active hydrothermal site (Figure 2). In situ sampling was complemented by 29 dredges (14 in 2007 and 15 in 2008; supporting information Table S1). Based on shipboard descriptions, the relative abundance of the lithologies recovered in dredges is shown in Figure 2, together with dredge samples from previous cruises. A representative suite of rock samples was selected for subsequent petrological examination using thin sections and geochemical analyses.

Major and trace element concentrations, presented in Table 1, were determined for 14 serpentinized peridotites, the dominant lithology encountered. These samples are representative of the different types of serpentinized peridotites throughout the Rainbow massif. Major element contents were determined by Inductively Coupled Plasma Optical Emission Spectrometry (ICP-OES; Thermo Elemental IRIS radial) at the SARM-CRPG (Nancy, France; http://helium.crpg.cnrs-nancy.fr/SARM/) after fusion with $LiBO_2$ and dissolution with HNO_3. Whole-rock minor and trace elements (Li, As, Sb, Co, Ni, Cu, Zn, Rb, Sr, Y, Cs, Ba, REE, Pb, Th, and U) were analyzed at Géosciences Montpellier (University Montpellier 2, France) on a ThermoFinnigan ELEMENT2 XR High Resolution (HR-)ICP-MS for all samples except for samples M7-PL10-7, M7-DR13-2, M8-DR5-1 and M8-DR9-1 that were analyzed using an Agilent 7700X quadrupole ICP-MS. The analytical procedure is described further in supporting information section S1 and Table S2.

Oxygen isotope compositions were determined on 14 representative bulk rock powders of serpentinized peridotites throughout the massif (supporting information Table S4). Isotopic compositions were performed at the Scottish Universities Environmental Research Centre (SUERC, UK) and are presented as δ values in ‰ relative to the Vienna Standard Mean Ocean Water (V-SMOW). The precision and accuracy of the measurements are ±0.2‰ (1σ) and NBS28 gives a $\delta^{18}O$ value of +9.6‰. Hydrogen isotope compositions were measured on the same 14 serpentinized peridotite samples (Table S4). They are given as δD values in ‰ relative to the Vienna Standard Mean Ocean Water (V-SMOW). Analytical precision of δD is ±3‰ (1σ) and NBS30 gives a δD value of −65‰ relative to V-SMOW. See details of analytical methods in supporting information section S2.

4. Results

4.1. Interpretation of Tectonic Framework From Available Geophysical Data

Bathymetry in Figure 1a suggests that, at its northern and southern tips, the massif is not structurally continuous with the oceanic crust formed along the adjacent segments to the east and west, which displays ridge-parallel abyssal hills. The summit of the massif is crosscut by a network of SW-NE trending fault scarps visible in both sonar imagery and bathymetry (Figure 1), which are up to 2 km in length and highly oblique

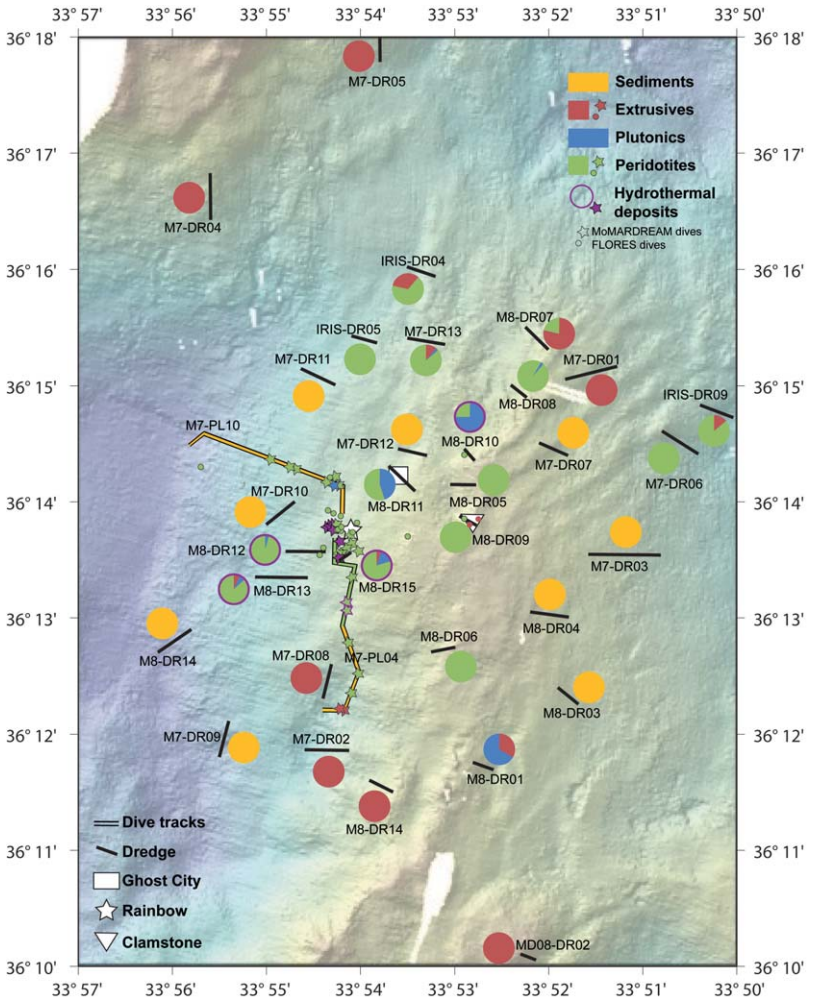

Figure 2. Location of dredges (DR) and dives (PL) done in the Rainbow massif area during the FLORES 1997 [*Fouquet et al*., 1998], IRIS 2001 [*Fouquet et al*., 2001], and MoMARDREAM (2007, 2008) cruises. The relative proportions of the recovered lithologies are illustrated in the pie charts.

to the spreading direction. On the eastern flank of the massif these fault scarps generally dip to the SE, while those on the western flank dip to the NW (Figures 1b–1d). Continuity and detailed geometry of scarps are not well constrained from the sonar data due to track geometry and illumination, but the largest fault scarps are discernible in the texture of the illuminated bathymetry and in the microbathymetry (Figures 1a and 1d). Vertical throws, documented by in situ diving observations and local microbathymetry, are up to ~20–30 m [*Lartaud et al*., 2010]. The sonar data also shows unfaulted seafloor as being textureless and displaying mainly low backscatter; we interpret this as sedimented seafloor. Minor patches with an irregular texture and high backscatter likely correspond to mass-wasting structures along the flanks of the massif.

The rift valley floors of the ridge segments, SW and NE of the massif, are also well sedimented (low backscatter), displaying both small seamounts and hummocky textures typical of volcanic constructions [e.g., *Smith and Cann*, 1990]. There is no tectonic structure in the acoustic images marking the transition from the flanks of the massif to contiguous rift valley floor. The bathymetry data show a clear break in slope (Figure 1), which is sharper on the western flank of the massif, with a more gradual transition on the eastern flank (Figure 1a).

Seismicity provides constraints on the present-day tectonic framework and stress orientation in the area. Seismic activity throughout the NTO (Figure 1a) is recorded both teleseismically between 1972 and the present time (NEIC catalog) and from hydroacoustic monitoring between 1999 and 2002 [*Smith et al*., 2003]. Focal mechanisms for two teleseismic events in the area (Figure 1a) show extension oblique to the

Table 1. Whole-Rock Chemical Analyses of Serpentinites From the Rainbow Massif

Cruise		M7	M7	M7	M7	M7	M7	M7	M8
Sample		M7-PL4–5	M7-PL4–6	M7-PL4–9	M7-PL4–14a	M7-PL4–14b	M7-PL10-7	M7-DR13-2	M8-DR5-1
Type of rock		Serpentinite	Serpentinite	Serpentinite	Serpentinite	Serpentinite	Serpentinite	Serpentinized peridotite	Serpentinized peridotite
Petrographic observations		Yellow-brown alteration corona around sample	Orange-brown veins	Mineralized	Orange-brown part	Green part	Red alteration patches + carbonates	Few olivine relicts + carbonates + orange-brown veins	Olivine and Pyroxene relicts
Location[a]			Hydrothermalized area	Rainbow field	Rainbow field	Rainbow field			
Lat		36.21	36.22	36.23	36.23	36.23	36.24	36.26	36.24
Long		−33.90	−33.90	−33.90	−33.90	−33.90	−33.91	−33.89	−33.88
Major Elements (wt %)									
SiO_2		40.64	35.88	34.00	41.23	41.34	34.99	38.28	36.88
Al_2O_3		0.65	0.37	0.88	0.62	0.55	0.90	0.69	0.59
Fe_2O_{3Tot}		9.28	7.10	19.74	6.08	6.14	9.44	7.30	7.16
FeO_{Tot}		8.35	6.39	17.76	5.48	5.53	8.50	6.57	6.44
MnO		0.12	0.08	0.13	0.07	0.07	0.09	0.16	0.09
CaO		0.04	2.20	<d.l.	<d.l.	<d.l.	1.49	0.18	2.96
MgO		34.54	37.51	31.51	37.80	38.27	36.06	39.28	37.20
K_2O		0.05	<d.l.	<d.l.	<d.l.	<d.l.	0.02	0.02	0.05
Na_2O		0.20	0.09	0.12	0.11	0.07	0.06	0.02	0.80
P_2O_5		<d.l.[d]	<d.l.	0.04	<d.l.	<d.l.	0.04	0.03	0.04
TiO_2		0.00	<d.l.	0.02	0.00	0.00	0.02	0.01	0.00
Total		85.50	83.22	86.44	85.92	86.45	83.11	85.97	85.77
LOI		14.24	15.65	12.28	12.75	13.50	14.03	13.57	14.26
$Fe^{2+}O$		3.50	2.39	7.68	2.86	2.77	1.82	1.30	3.06
Fe^{3+}/Fe_{Tot}		0.581	0.626	0.568	0.478	0.499	0.786	0.802	0.525
Trace Elements (ppm)									
Co	*ppm*	116	87	237	101	98	135	143	99
Ni	*ppm*	2096	1889	2854	1786	1841	1519	2110	2012
Cu	*ppm*	37.6	13.4	40.2	2.5	10.7	55.7	77.4	1.5
Zn	*ppm*	128	41	1661	32	31	83	62	36
Y	*ppm*	2.327	0.313	0.566	0.851	0.214	0.370	1.528	0.022
Pb	*ppm*	1.998	0.018	0.100	0.477	0.425	0.085	3.350	0.132
As	*ppm*	5.76	<d.l.	<d.l.	<d.l.	<d.l.	21.23	22.61	0.05
Sb	*ppm*	0.129	0.167	0.117	0.232	0.060	0.680	0.350	0.010
Li	*ppm*	7.30	0.42	0.09	9.85	10.10	0.57	2.16	1.17
Rb	*ppm*	1.276	0.046	0.053	0.149	0.158	0.128	0.082	0.104
Cs	*ppm*	0.078	0.003	0.002	0.008	0.009	0.003	0.004	0.020
Sr	*ppm*	10.4	488.0	2.5	4.1	3.9	284.1	13.0	452.6
Ba	*ppm*	0.863	1.863	0.297	0.508	0.712	1.437	6.122	1.145
Th	*ppm*	0.0054	0.0232	0.0321	0.0071	0.0097	0.0080	0.3270	0.0030
U	*ppm*	0.346	0.588	0.681	0.694	0.501	0.831	1.050	1.091
La	*ppb*	314.3	77.8	20188.0	249.3	207.7	93.0	1581.0	16.0
Ce	*ppb*	883.0	121.8	17955.7	591.2	303.4	167.0	4916.0	34.0
Pr	*ppb*	126.8	19.3	1032.6	74.9	32.5	19.0	336.0	4.0
Nd	*ppb*	728.2	89.6	2388.4	364.8	134.9	84.0	1438.0	12.0
Sm	*ppb*	250.3	21.4	222.2	127.0	31.0	19.0	300.0	3.0
Eu	*ppb*	57.5	5.3	21.9	130.9	194.4	6.0	71.0	2.0
Gd	*ppb*	328.3	31.9	402.8	185.0	44.3	32.0	357.0	3.0
Tb	*ppb*	53.3	5.1	30.2	28.7	6.1	6.0	52.0	0.0
Dy	*ppb*	354.0	35.8	115.4	175.6	39.0	47.0	324.0	3.0
Ho	*ppb*	61.0	8.4	17.3	30.8	7.1	12.0	65.0	1.0
Er	*ppb*	194.7	26.7	73.8	77.1	21.0	40.0	189.0	4.0
Tm	*ppb*	30.1	4.5	9.9	10.3	3.3	6.0	28.0	1.0
Yb	*ppb*	192.7	34.9	67.1	62.5	24.9	51.0	176.0	13.0
Lu	*ppb*	33.2	7.3	12.0	10.2	5.1	10.0	30.0	3.0
REE pattern		Type 3	Type 3	Type 3	Type 1	Type 1	Type 3	Type 3	Type 1
Eu/Eu*		0.6	0.6	0.2	2.6	16.0	0.7	0.7	2.0
Isotopic Composition and Serpentinization Temperature (Ts) Estimates									
$\delta_{18}O$	‰	2.73	3.24	0.77		3.14	3.7	3.9	4.6
δD	‰	−60	−58	−55		−70	−72	−67	−71
Average Tsw[b]	°C	220	206	289		210	195	191	177
Average THF[c]	°C			408					

Table 1. Continued

Cruise		M8	M8	M8	M8	M8	M8	M8
Sample		M8-DR6-1a	M8-DR6-1b	M8-DR6-1c	M8-DR6-3	M8-DR8-3	M8-DR8-4	M8-DR8–22
Type of rock		Serpentinized peridotite	Serpentinized peridotite	Serpentinized peridotite	Serpentinite	Serpentinite	Serpentinite	Serpentinite
Petrographic observations		Almost fully serpentinized (few Pyroxene relicts)	Moderately serpentinized (Olivine and Pyroxene relicts)	Slightly serpentinized (Olivine and Pyroxene relicts)			Dunitic protolith	
Location[a]								
Lat		36.21	36.21	36.21	36.21	36.25	36.25	36.25
Long		−33.89	−33.89	−33.89	−33.89	−33.87	−33.87	−33.87
Major Elements (wt %)								
SiO_2		37.41	38.72	38.52	39.11	38.41	39.23	37.67
Al_2O_3		0.58	0.58	0.53	0.69	0.60	0.19	0.63
Fe_2O_{3Tot}		7.08	7.23	7.37	7.20	7.90	8.41	8.42
FeO_{Tot}		6.37	6.50	6.63	6.48	7.11	7.57	7.58
MnO		0.10	0.09	0.11	0.04	0.06	0.05	0.08
CaO		3.94	1.66	0.40	0.03	0.21	0.08	1.04
MgO		36.20	37.73	39.63	38.40	38.30	38.78	37.29
K_2O		<d.l.	<d.l.	<d.l.	<d.l.	<d.l.	<d.l.	<d.l.
Na_2O		0.08	0.05	0.02	0.10	0.06	0.13	<d.l.
P_2O_5		<d.l.	0.05	0.06	0.04	<d.l.	0.04	0.06
TiO_2		<d.l.	<d.l.	<d.l.	0.01	0.00	<d.l.	<d.l.
Total		85.39	86.11	86.64	85.61	85.55	86.91	85.19
LOI		15.44	13.08	12.72	13.72	13.70	13.99	14.37
$Fe^{2+}O$		2.72	3.35	3.77	1.40	1.95	2.09	2.07
Fe^{3+}/Fe_{Tot}		0.573	0.485	0.431	0.784	0.726	0.724	0.727
Trace Elements (ppm)								
Co	*ppm*	86	109	114	75	100	130	83
Ni	*ppm*	1663	2023	2137	1790	1959	2119	1638
Cu	*ppm*	1.0	1.5	1.3	8.7	1.5	0.6	4.4
Zn	*ppm*	29	34	40	26	41	38	44
Y	*ppm*	0.025	0.023	0.017	0.276	0.052	0.048	0.118
Pb	*ppm*	<d.l.	<d.l.	<d.l.	<d.l.	<d.l.	0.074	0.030
As	*ppm*	0.07	<d.l.	<d.l.	1.72	1.45	3.25	0.07
Sb	*ppm*	0.024	0.003	0.004	0.079	0.047	0.068	0.032
Li	*ppm*	1.34	0.87	0.77	2.20	0.17	0.04	0.11
Rb	*ppm*	0.058	0.083	0.061	0.061	0.030	0.036	0.008
Cs	*ppm*	0.007	0.014	0.010	0.006	0.004	0.005	0.000
Sr	*ppm*	1429.4	196.9	1.3	2.0	2.1	14.7	360.7
Ba	*ppm*	2.467	0.716	0.257	0.222	0.292	0.162	0.409
Th	*ppm*	0.0020	0.0012	0.0009	0.0061	0.0001	0.0011	0.0002
U	*ppm*	1.071	0.554	0.001	0.680	0.715	0.407	0.988
La	*ppb*	10.9	7.7	7.4	116.7	16.4	33.5	22.5
Ce	*ppb*	21.1	14.2	15.3	278.5	34.8	88.1	47.0
Pr	*ppb*	2.0	1.4	1.3	32.2	4.3	8.2	5.5
Nd	*ppb*	7.8	4.8	5.0	155.4	20.1	35.6	28.1
Sm	*ppb*	1.5	1.2	1.2	36.1	5.0	6.4	7.6
Eu	*ppb*	1.8	1.0	0.6	102.3	22.1	10.9	26.1
Gd	*ppb*	1.9	1.5	1.0	51.4	6.5	8.7	10.9
Tb	*ppb*	0.2	0.2	0.1	6.9	1.1	1.1	2.1
Dy	*ppb*	2.0	1.3	1.1	46.0	7.0	7.0	16.7
Ho	*ppb*	0.8	0.6	0.5	9.4	1.5	1.3	4.0
Er	*ppb*	4.1	3.8	3.0	29.8	6.1	4.4	16.8
Tm	*ppb*	1.1	1.1	1.1	5.0	1.4	0.8	3.5
Yb	*ppb*	13.7	14.1	11.7	36.8	14.3	7.3	33.5
Lu	*ppb*	3.8	3.7	3.2	7.3	3.2	2.1	7.7
REE pattern		Type 1	Type 1	Type 1	Type 1	Type 1	Type 1	Type 1
Eu/Eu*		3.3	2.2	1.5	7.3	11.8	4.5	8.8
Isotopic Composition and Serpentinization Temperature (Ts) Estimates								
$\delta_{18}O$	‰				2.59			1.22
δD	‰				−69			−59
Average Tsw[b]	°C				224			266
Average THF[c]	°C							

Table 1. Continued

Cruise		M8	M8	M8	M8	M8	M8	M8
Sample		M8-DR9-1a	M8-DR10–13	M8-DR11-6	M8-DR12-1a	M8-DR12-4a	M8-DR13-1a	M8-DR15-1b
Type of rock		Serpentinite	Serpentinite	Serpentinite	Serpentinite	Serpentinite	Serpentinite	Serpentinite
Petrographic observations		Carbonates + red alteration corona around sample	Dunitic protolith + red alteration veins		Mineralized	Impregnated texture yellow-green alteration	Yellow-green alteration	
Location[a]		Clamstone	Hydrothermalized area	Ghost City	Rainbow stockwork	Rainbow stockwork	Rainbow stockwork	Rainbow stockwork
Lat		36.23	36.24	36.24	36.23	36.23	36.22	36.23
Long		−33.88	−33.88	−33.89	−33.91	−33.91	−33.92	−33.90
Major Elements (wt %)								
SiO_2		36.70	35.69	38.94	37.80	38.09	38.63	39.38
Al_2O_3		1.00	1.19	0.61	0.54	0.64	0.91	0.74
Fe_2O_{3Tot}		9.25	10.13	7.81	16.49	9.08	8.10	5.00
FeO_{Tot}		8.32	9.12	7.03	14.84	8.18	7.29	4.50
MnO		0.04	0.07	0.06	0.06	0.08	0.05	0.08
CaO		0.15	3.24	0.17	0.07	<d.l.	<d.l.	<d.l.
MgO		33.87	35.24	38.84	32.81	38.51	38.86	39.32
K_2O		0.18	<d.l.	<d.l.	0.05	<d.l.	<d.l.	<d.l.
Na_2O		0.89	0.09	0.07	0.17	0.13	0.15	0.12
P_2O_5		0.02	0.04	0.04	0.02	0.04	0.03	<d.l.
TiO_2		0.03	0.03	<d.l.	0.03	0.01	0.02	0.01
Total		82.12	85.72	86.54	88.03	86.57	86.76	84.64
LOI		17.31	15.10	14.24	12.07	13.88	14.13	16.55
$Fe^{2+}O$		1.47	2.34	3.34	5.33	2.33	1.53	1.09
Fe^{3+}/Fe_{Tot}		0.823	0.743	0.525	0.641	0.715	0.790	0.758
Trace Elements (ppm)								
Co	*ppm*	61	108	94	98	98	43	72
Ni	*ppm*	1430	1260	1783	2075	1574	1154	1903
Cu	*ppm*	1.8	13.3	16.3	57.6	19.6	63.1	0.3
Zn	*ppm*	29	41	64	53	171	71	37
Y	*ppm*	0.099	0.452	0.148	0.125	0.920	1.066	0.058
Pb	*ppm*	0.324	<d.l.	0.526	0.308	0.155	0.046	0.043
As	*ppm*	19.43	0.08	9.05	0.55	5.51	5.46	0.88
Sb	*ppm*	0.640	0.046	0.129	0.140	0.055	0.064	0.037
Li	*ppm*	2.04	0.48	1.58	14.78	0.11	0.44	0.10
Rb	*ppm*	1.528	0.142	0.046	0.360	0.042	0.044	0.033
Cs	*ppm*	0.172	0.008	0.002	0.014	0.004	0.002	0.002
Sr	*ppm*	8.7	1217.7	2.9	12.6	1.9	2.2	1.9
Ba	*ppm*	0.784	0.687	0.361	1.035	0.083	0.120	0.101
Th	*ppm*	0.0430	0.0138	0.0015	0.0100	0.0137	0.0469	<d.l.
U	*ppm*	0.493	0.930	0.722	0.281	0.692	0.411	0.706
La	*ppb*	36.0	75.4	55.2	555.0	140.2	270.2	63.4
Ce	*ppb*	105.0	164.8	63.7	664.0	476.6	790.4	115.1
Pr	*ppb*	15.0	19.3	9.3	55.0	65.5	107.9	8.7
Nd	*ppb*	73.0	85.6	39.8	195.0	365.5	534.5	22.7
Sm	*ppb*	21.0	26.5	6.0	35.0	102.3	135.4	1.8
Eu	*ppb*	6.0	13.8	20.1	23.0	42.8	62.8	13.2
Gd	*ppb*	21.0	47.4	10.4	39.0	158.1	199.8	3.2
Tb	*ppb*	4.0	8.8	1.4	4.0	23.4	29.6	0.4
Dy	*ppb*	26.0	64.6	10.7	17.0	160.5	212.8	4.6
Ho	*ppb*	5.0	15.5	2.8	4.0	31.2	41.7	1.7
Er	*ppb*	15.0	53.2	12.0	13.0	96.0	129.2	9.2
Tm	*ppb*	3.0	9.6	2.5	3.0	14.3	20.2	2.3
Yb	*ppb*	20.0	75.2	22.5	21.0	96.9	141.3	22.6
Lu	*ppb*	4.0	16.2	5.5	5.0	15.4	24.8	5.3
REE pattern		Type 2	Type 2	Type 1	Type 1	Type 2	Type 2	Type 1
Eu/Eu*		0.9	1.2	7.7	1.9	1.0	1.2	16.6
Isotopic Composition and Serpentinization Temperature (Ts) Estimates								
$\delta_{18}O$	‰	5.1	1.92	3.04	2.4			2.16
δD	‰	−64	−62	−72	−55			−57
Average Tsw[b]	°C	166	244	211	229			236
Average THF[c]	°C				305			

[a]Location corresponds to the coordinate of the central point of a dredge line (-DR) or to the exact position of sample collection during a dive (-PL).

[b]Tsw is the average temperature of serpentinization calculated from the four available thermometers of *Saccocia et al.* [2009], *Savin and Lee* [1988], *Wenner and Taylor* [1971], and *Früh-Green et al.* [1996], using seawater as the serpentinizing fluid (also see Table S1).

[c]THF is the average temperature of serpentinization calculated from the four available thermometers of *Saccocia et al.* [2009], *Savin and Lee* [1988], *Wenner and Taylor* [1971], and *Früh-Green et al.* [1996], using a hydrothermal fluid as the serpentinizing fluid (also see Table S1).

<d.l. = below detection limit.

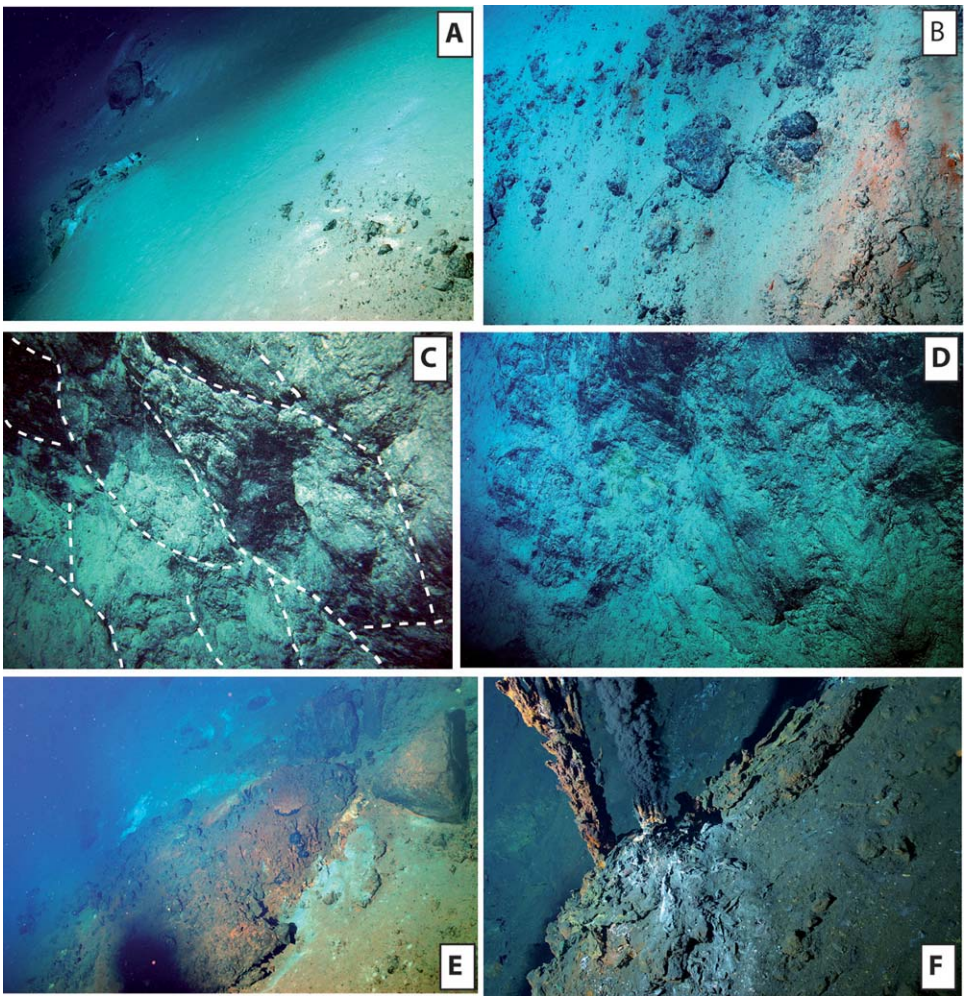

Figure 3. In situ observations during dive M7-PL4 that explored a 6 km N-S transect south of the active Rainbow field. The distance to the active site decreases from Figures 3a–3f. (a, b) Sediment cover with serpentinized peridotites outcropping at slope breaks. White-brown deposits within serpentinite outcrops suggest a pervasive hydrothermal activity several km away from the active site, at least along west dipping decametric cliffs (green stars circled in violet along M7-PL4 dive in Figure 2). This area is less extensively covered by sediment than the southern part of the dive (yellow line with green or red stars on M7-PL4 dive in Figure 2). (c, d) N-S subvertical cliffs of ultramafic rocks observed over 1.5 km south of the active field. They display both distributed (elongated metric blocks: Figure 3c) and localized (striated fault planes: Figure 3d) deformation structures. They both indicate an oblique displacement along these faults, probably extensive. (e, f) Photographs of the active site showing hydrothermalized serpentinite blocks characterized by an (e) orange-brown alteration crust and (f) active sulfide chimneys located on a steep, west dipping, slope.

spreading direction (~30°C clockwise), indicating important stress rotation likely associated with mechanical coupling along this nontransform discontinuity [e.g., *Grindlay and Fox*, 1993]. The orientation of extension derived from the seismicity is also consistent with that of the oblique, extensional fault network identified in the sonar images (Figures 1b and 1c). Hydroacoustic events, corresponding to earthquakes of magnitude 3–3.5 or higher [e.g., *Smith et al.*, 2002], do not provide any information on stress orientations but indicate that this area is tectonically active.

4.2. In Situ Observations From MoMARDREAM Cruises

Nautile dives M7-PL4 and M7-PL10 are ~6 km long and provide observations of the western flank of the massif up to the active hydrothermal site (Figure 2). Observations confirm an extensive sedimentary cover south and northwest of the active Rainbow site, down to the rift valley as previously deduced from TOBI data. It considerably hinders geological observations and sampling of this region, which is thus limited to a few outcrops at slope breaks (Figure 3a). Evidence of pervasive hydrothermal activity through the sediment cover is suggested by the white and brown colors at ultramafic outcrops, likely corresponding to hydrothermal staining (Figures 3a and 3b), which are observed up to ~2 km south of the active field (violet outline

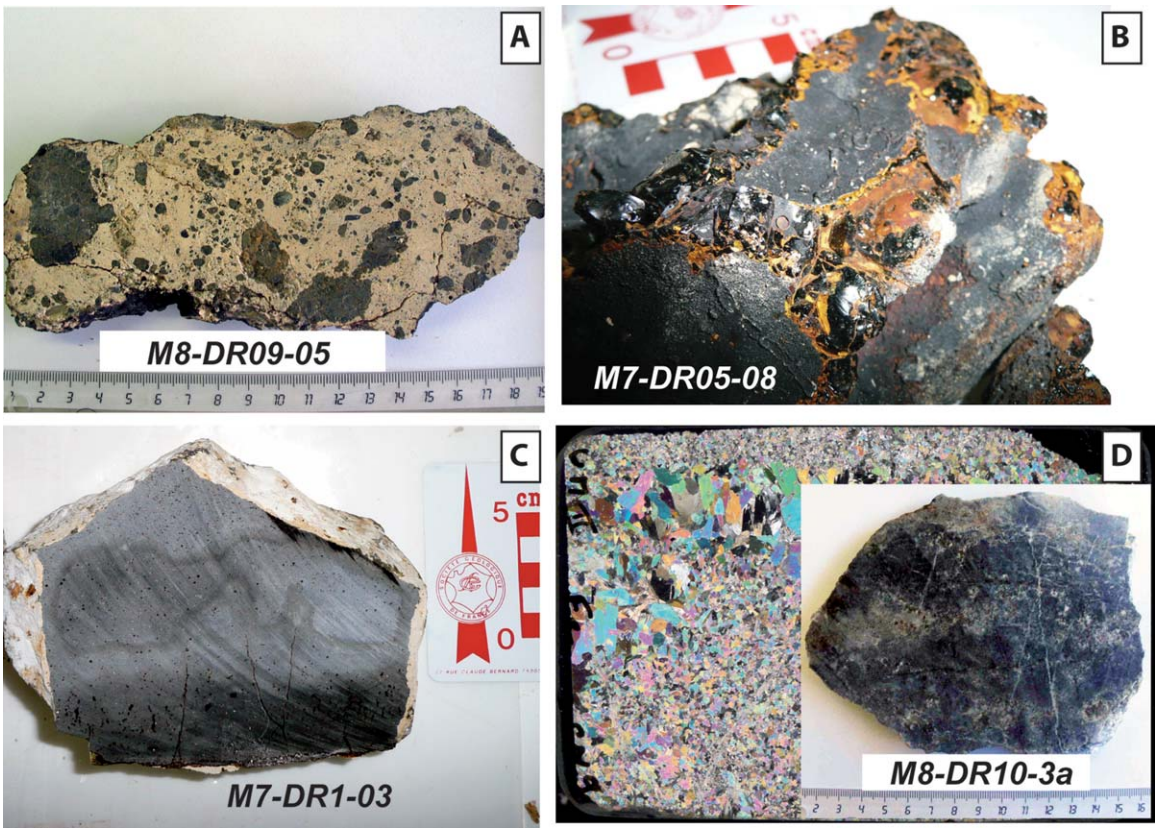

Figure 4. Carbonate-cemented breccias and extrusive rocks. (a) Serpentinites enclosed in carbonate cement from the Clamstone fossil site. (b) Fresh basaltic glass, (c) more altered basalts. (d) Epidosite sample: macroscopic sample and scanned thin section (45 × 30 mm; cross-polarized light).

around green stars in Figure 2). These hydrothermal markers coincide with steeper slopes and the occurrence of decametric west facing cliffs. Closer to the active field (<1.5 km south), ~20 m high subvertical cliffs of ultramafic rocks display both distributed (elongated metric blocks; Figure 3c) and localized (striated faults planes; Figure 3d) deformation. The active hydrothermal field lies above similar fault scarps, on a steep slope partially covered by sediments (Figures 3e and 3f).

4.3. Occurrences and Petrography of Sampled Lithologies

A large variety of lithologies was recovered, including variously altered extrusive (basalt), plutonic (primarily gabbroic rocks and diabase), and ultramafic residual mantle (serpentinized peridotite) rocks, in addition to hydrothermal deposits, carbonates, and pelagic sediments (Figure 2).

4.3.1. Sediments and Carbonates

As observed during dives, the Rainbow massif displays a widespread cover of pelagic sediments. They can be either soft (supporting information Figure S1a, inset) or indurated (Figure S1a) and lithified with a Mn coating and bioturbations (Figure S1b) as in dredges M8-DR01, M8-DR03, M8-DR04, M8-DR09, and M8-DR11.

Carbonates have been sampled together with ultramafic and magmatic rocks in dredges M8-DR11 and M8-DR09, at the Ghost City and Clamstone fossil vent sites, respectively. They have been described in detail by *Lartaud et al.* [2010, 2011] as being poor in metals, and enclosing mussel shells and pelagic fossils, characteristics of an ancient low-T, alkaline, hydrothermal activity (Figure S1c). The authigenic carbonate fraction provided formation ages for the two serpentinite-hosted sedimented vent sites: U/Th dating yielded ~110 kyr for the Ghost City site [*Lartaud et al.*, 2011] and ^{14}C dating yielded ~25 kyr for the Clamstone site [*Lartaud et al.*, 2010]. Carbonates are also observed cementing breccias (Figure 4a) of ultramafic and/or magmatic clasts (M8-DR09, M8-DR10, and M8-DR15).

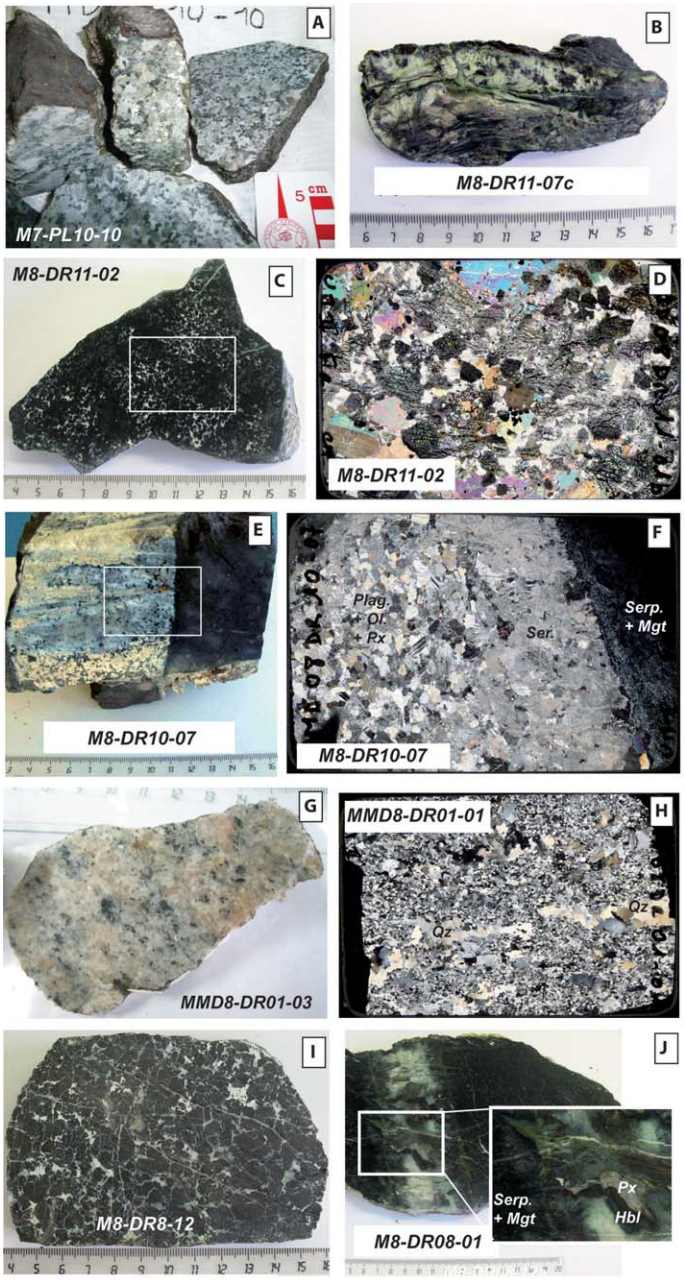

Figure 5. Examples of plutonic rocks from the Rainbow massif: (a) Coarse-grained gabbronorite. (b) Deformed gabbro. (c) Troctolite. (d) Thin section scan corresponding to the white rectangle in Figure 5c. (e) Olivine gabbro (yellow-gray) displaying a sharp primary contact with a serpentinized peridotite. (f) Thin section scan corresponding to the white rectangle in Figure 5e. (g) Undeformed plagiogranite. (h) Plastically deformed plagiogranite. (i) Chromitite. (j) Gabbroic veinlet crosscutting a serpentinized peridotite. Hbl = hornblende; Mgt = magnetite; Ol. = olivine; Plag. = plagioclase; Px = pyroxene; Qz = quartz; Ser. = sericite; Serp. = serpentine.

4.3.2. Magmatic Rocks

Dikes and volcanics are fine-grained diabases and microcrystalline basalts with fresh glass (Figure 4b) and rare millimetric vacuoles (Figure 4c), outcropping preferentially on the northern and southern edges of the Rainbow massif, and to the NW, on the conjugate flank across the nodal basin (Figure 2). One epidosite has been collected (dredge M8-DR10 in Figures 4d), indicating localized, high-T fluid discharge on the NE flank of the massif, away from the major active site (violet circle around M8-DR10 in Figure 2). Only very minor occurrences of extrusive rocks occur at the massif center; in two MoMARDREAM dredges (M8-DR13 and M8-DR15) and near the Clamstone site during previous dives (FLORES cruise) [*Fouquet et al*., 1998], representing less than 10% of the collected rocks (Figure 2).

Mafic plutonic rocks were found in six MoMARDREAM dredges, and along Nautile dive track M7-PL10. They are troctolites (Figures 5c and 5d), olivine gabbros (Figures 5e and 5f), gabbros, and gabbronorites (Figures 5a and 5b) and are associated with serpentinized peridotites throughout the core of the massif (Figure 2), except in dredge M8-DR01 where they are exclusively associated with extrusive rocks. Sharp primary contacts between serpentinized peridotites and gabbros (Figure 5e) or gabbroic veins (Figure 5j) are observed, especially in dredge M8-DR08. The bulk of these rocks are undeformed, but some gabbros show plastic deformation of pyroxenes, and there are some ductile to brittle deformation bands in the greenschist facies (Figure 5b). Samples with more than 90% chromite (Figure 5i) were recovered in dredge M8-DR08, sometimes in sharp contact with highly altered mantle rocks. Dredge M8-DR01 recovered three granite and plagiogranite samples (Figures 5g and 5h) displaying variable textures, from macrocrystalline magmatic textures (Figure 5g) to plastically deformed textures exhibiting quartz ribbons that result from high-T solid-

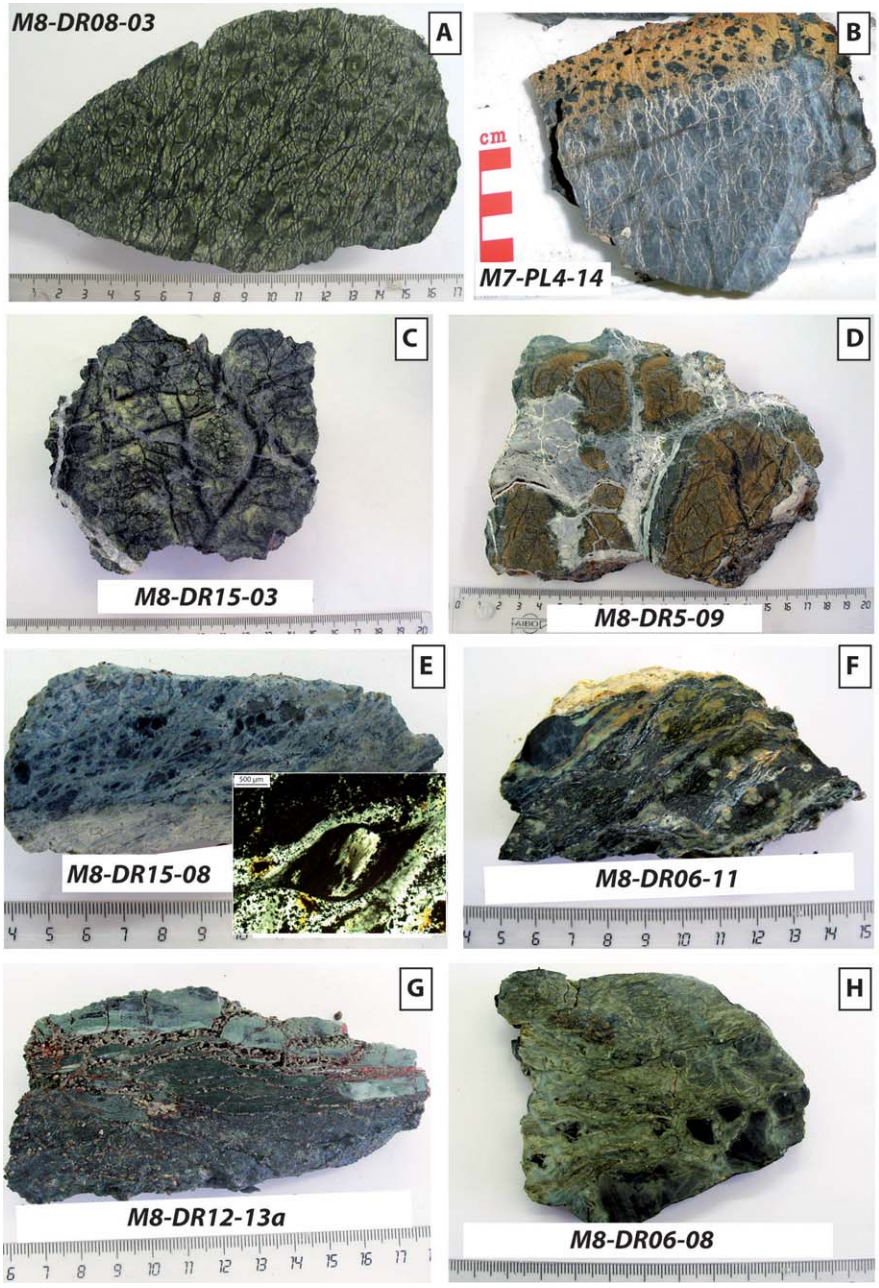

Figure 6. Examples of mantle rocks from the Rainbow massif: (a) serpentinized harzburgite, (b) serpentinized harzburgite collected at the active Rainbow field (Figure 3e) and displaying an orange-brown alteration crust, (c) serpentinized dunite crosscut by white carbonate veins, (d) highly serpentinized impregnated harzburgite with orange-brown alteration, (e) mylonitic peridotite with relicts of plastically deformed pyroxene (inset), altered to a serpentine and chlorite assemblage, highly enriched in magnetite, (f) foliated serpentinite displaying a first stage of plastic deformation, recorded by elongated pyroxene phenocrysts, and overprinted by a second deformation stage in the semibrittle field of serpentine-chlorite, (g) foliated serpentinite showing slickensided surfaces formed by localized syntectonic crystal growth of chlorite-serpentine, (h) foliated serpentinite deformed in the semibrittle field. Foliation is mainly highlighted by chlorite and serpentine.

state deformation (Figure 5h). Plutonic rocks are variably altered under greenschist-facies conditions, with secondary assemblages dominated by actinolite and chlorite. Olivine-poor lithologies are well preserved from retrograde metamorphism, which mainly occurs as a slight albitization of plagioclase. Contact with serpentinized peridotite seems to locally enhance gabbro alteration marked by sericite formation after feldspars (Figure 5f). Gabbroic veins present a partial amphibolite-facies recrystallization of pyroxene to hornblende (e.g., Figure 5j, inset), overprinted by greenschist-facies minerals (mainly chlorite and actinolite). Where present, olivine is the most altered mineral. It is partially replaced by serpentine and magnetite (Figures 5d and 5f), which

contributes, together with feldspars, to the relatively higher alteration degree of troctolites. In chromitites, chromite is almost fresh (Figure 5i; Cr# (Cr/(Cr + Al)) atomic ratio = 0.51; supporting information Table S3) while plagioclase is fully replaced by chlorite. Granitoids have undergone the least alteration.

4.3.3. Mantle Rocks

Mantle rocks form the most abundant rock type sampled. They are highly serpentinized, with very variable textures. They occur throughout the massif, except in the extreme south (Figure 2). We have primarily recovered harzburgites (Figures 6a and 6b), and to a lesser extent dunites (Figures 6c and 6d). Some samples are crosscut by gabbroic veins (e.g., Figure 5j) or irregular gabbroic intrusions, which are altered to greenschist-facies assemblages (tremolite-talc-chlorite, e.g., Figure 6d). Mylonitic peridotites displaying evidence of an early phase of plastic deformation, recorded by pyroxene phenocrysts, have been sampled in dredges M8-DR06 and M8-DR15 (Figures 6e and 6f). Plastic deformation is overprinted by hydrated phases, mainly serpentine and chlorite. Sample M8-DR15-08, located very close to the active hydrothermal site (Figure 2), is also highly enriched in magnetite, pyrite, and hydrogarnet (Figure 6e, inset). Dredges M8-DR06 and M8-DR12 recovered serpentinites displaying cataclastic deformation and syntectonic growth of serpentine-chlorite assemblages (Figure 6h). Serpentinites observed and collected on N-S fault scarps during dive M7-PL4 (Figures 3c and 3d) show slickenside surfaces, indicating shear localization mainly accommodated by syntectonic crystal growth of serpentine (Figure 6g) or of chlorite-serpentine-tremolite ± talc assemblages (Figure 7f).

Peridotite is the most altered lithology, with most of the samples displaying undeformed primary textures overprinted by static serpentinization textures (mesh and bastite textures; Figures 7a and 7b) and late veining (e.g., chrysotile veins; Figure 7a). Serpentinites are commonly green to yellow-green (Figures 5e, 6a–6d, and 7g), with a few relicts of primary minerals (Figures 7a and 7b). Clinopyroxene is uncommon in the studied sample, and is unaffected by hydration. The least serpentinized samples, referred to as serpentinized peridotites in Table 1, come from locations where peridotites were not associated with intrusive lithologies (M8-DR05 and M8-DR06). Some samples coming from the high-T hydrothermal vent field area (Figure 2) show an orange alteration forming either a crust or pervasive veinlets (orange serpentinites, e.g., Figures 3e and 6b). This alteration is similar to the orange-brown alteration pattern often observed in partially or fully serpentinized samples all over the massif (orange-brown serpentinites, e.g., Figures 6d and 7g), especially those containing carbonates. Red, hematite-rich alteration coronas, or red iron-rich patches disseminated around olivine relicts when present, can also be observed in some samples (Figures 7g and 7h). Serpentinization textures can either be crosscut by late Ca-rich carbonate veins (Figure 6c), or be more pervasively carbonated (Figures 7c–7e), with carbonate precipitation along magnetite veinlets (Figure 7d) and the formation of Ca-rich, Si-Mg-poor metasomatic zones in mesh textures (Figure 7e). Carbonates are also observed on localized fault planes where they separate the previously grown fibrous minerals (Figure 7f).

In addition to sulfide deposits and chimneys (Figure 8a), the active hydrothermal site and its stockwork are characterized by Si-enriched (steatite type; Figure 8e) and mineralized serpentinites (Figures 8b–8d). The latter are collected over a large area, extending up to ~2 km south and west of the active vent field (violet outline and stars in Figure 2: M7-PL4, M8-DR12, M8-DR13, and M8-DR15). Similar samples were also found ~5 km to the northeast in dredge M8-DR10. These high-T hydrothermal samples were recovered along a NE-SW profile, parallel to the oblique structures (faults and fissures visible in the bathymetry and sonar imagery, Figure 1). This high-T hydrothermal stage of serpentinite alteration overprints the previous pseudomorphic serpentinization textures (Figures 8f–8i). It is characterized by millimetric to micrometric sulfide mineralization disseminated within the samples (Figures 8b–8d and 8g–8i). It can be associated with partial recrystallization of serpentine textures to a Fe-enriched serpentine (pleochroic brown-green phase in Figure 8f, and light gray in Figure 8g) that forms a corona around serpentinized pyroxene, or by the development of a highly porous mesh texture enriched in sulfides (Figures 8g–8i). The latter is a texture of serpentine corrosion that has already been described by *Marques et al*. [2007] within the serpentinite stockwork of semi-massive sulfide rocks from the Rainbow vent field. Sulfide precipitations tend to localize along fibrous shear zones and faults planes, when present (Figure 8i).

4.4. Geochemistry of Serpentinites

4.4.1. Major Elements and Metals

Whole-rock major element compositions of the sampled serpentinized peridotites (Table 1) plot in the field of refractory abyssal peridotites (Figure 9a), except for their iron content. The Rainbow serpentinites display

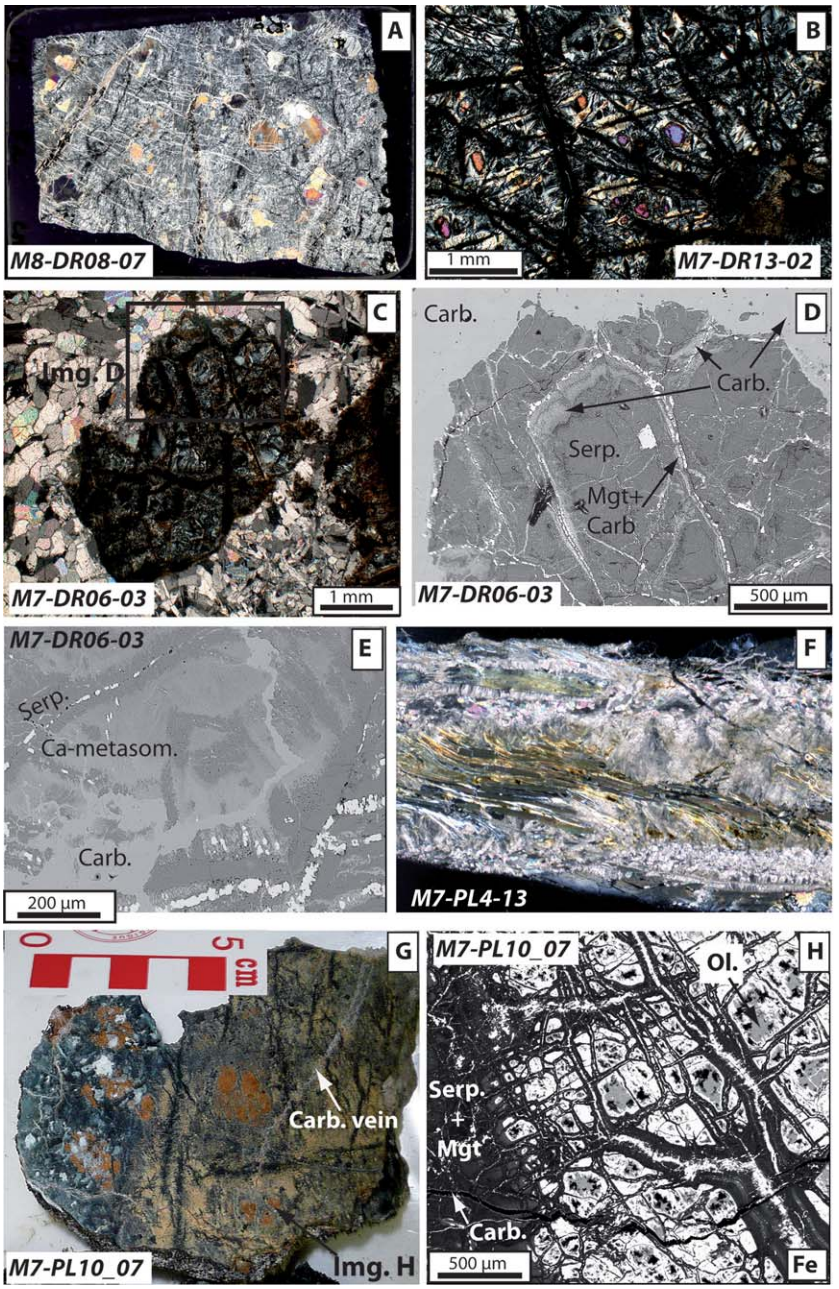

Figure 7. (a, b) Photomicrograph of a scanned thin section (45 × 30 mm; cross-polarized light) of partially serpentinized peridotites. (a) Pyroxene can be relatively preserved from hydration, (b) while olivine relicts are usually scarce. (c) Photomicrograph (cross-polarized light) of a serpentinized and carbonated peridotite, with location of Figure 7d. (d) Backscattered SEM image of the carbonated serpentinite in Figure 7c. Carbonates develop as massive veins and scattered grains within the mesh texture of serpentinization. Mgt = magnetite. (e) Backscattered SEM image of the carbonated serpentinite in Figure 7c, showing the pervasive Ca-metasomatism associated with the carbonation process. (f) Photomicrograph (cross-polarized light) of a foliated serpentinite collected on N-S fault scarps during dive M7-PL4 (Figures 3c and 3d) and showing slickensided surfaces formed by localized syntectonic crystal growth of chlorite-serpentine-tremolite, plus talc. Carbonates precipitate within the fibrous fault plane. (g) Red alteration corona, rich in iron, around olivine relicts, with location of Figure 7h. (h) SEM-EDS image of iron relative content of the serpentinite sample in Figure 7g, highlighting the iron-rich coronas (white) around olivine relicts (gray). Carb. = carbonate; Mgt = magnetite; Ol. = olivine; Serp. = serpentine.

highly variable iron content (FeO_{Tot} = 6.37–17.76 wt %; Figure 9b). Most of the Fe-rich samples plot within the field of impregnated abyssal peridotites defined by ODP Leg 209 samples from Sites 1270 and 1271 [*Paulick et al*., 2006]. Three serpentinites (M8-DR10–13, M7-PL4–09, and M8-DR12-1a) plot outside this field (Table 1 and Figure 9b). They were located near and within the stockwork of the active hydrothermal site. Samples M7-PL4-09 and M8-DR12-1a contain abundant sulfide (Figures 8f–8i). M7-PL4-09 is the most

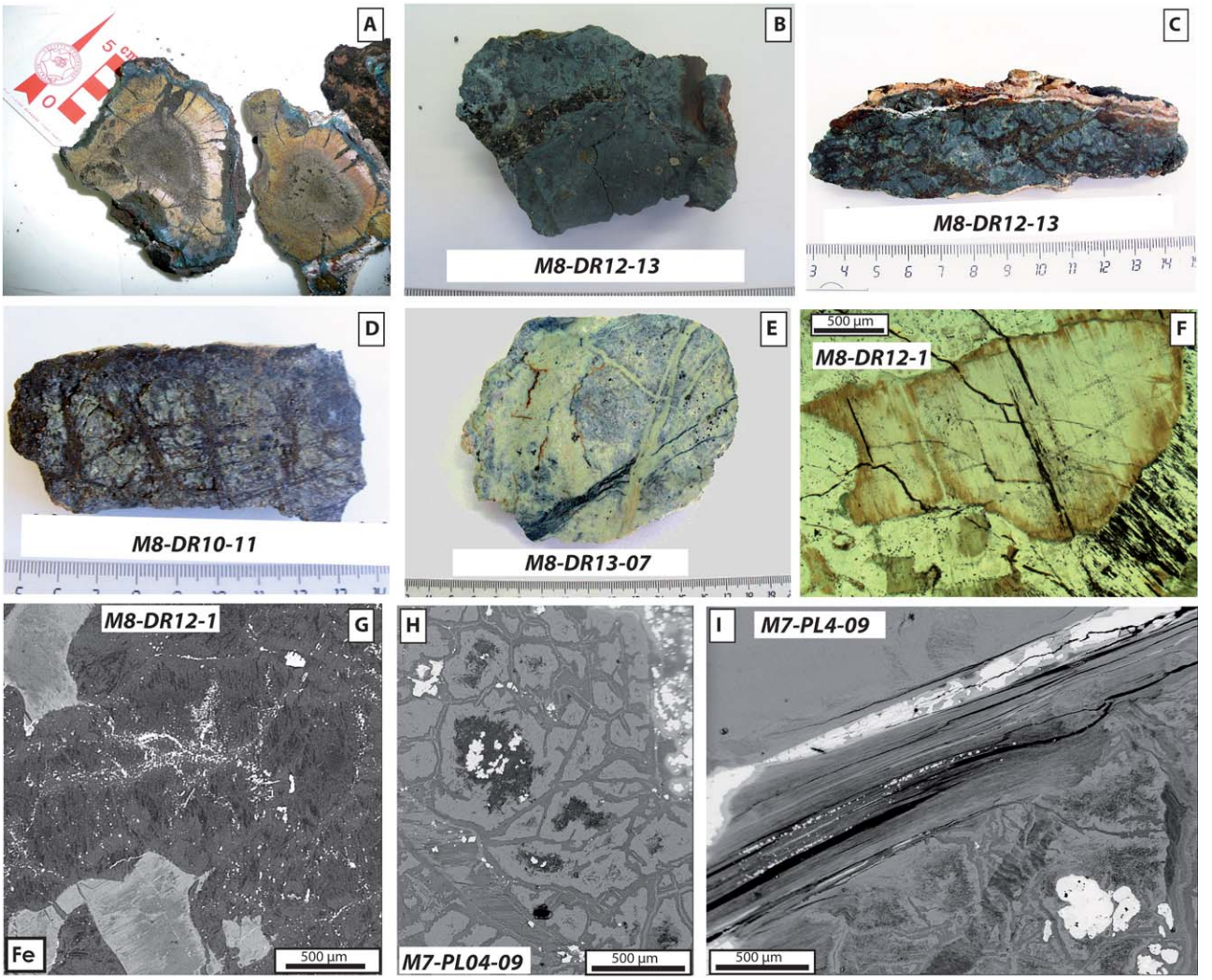

Figure 8. Hydrothermalized samples from the Rainbow vent field area: (a) cross section of sulfide chimneys; (b–d) mineralized serpentinites characterized by sulfide veinlets; (e) silicified serpentinites from the Rainbow stockwork; (f) photomicrograph of a pervasively mineralized serpentinite characterized by the occurrence of an iron-rich corona around serpentinized pyroxenes. (g) SEM image of millimetric to micrometric sulfide mineralizations disseminated within the sample in Figure 8f. (h, i) Photomicrographs of a pervasively mineralized serpentinite characterized by localized sulfide precipitation within (h) pseudomorphic textures or (i) along fracture planes.

mineralized serpentinite, and the richest in other metals, especially Zn (1661 ppm), and, to a lesser extent, Co (237 ppm) and Cu (40 ppm). Some samples from regions where evidence of hydrothermalism have been observed (violet outline and stars in Figure 2) also tend to show higher contents of Cu or Zn (e.g., M8-DR12-4 and M8-DR13-1 with Cu $>$ 19.5 ppm and Zn $>$ 70 ppm) but this enrichment in metals is not systematic (e.g., M8-DR15-1 or M8-DR10-13). This is also true for the samples collected in the immediate vicinity of the Rainbow hydrothermal vent field (e.g., samples M7-PL4-14, upper right corner of Figure 3e). These serpentinites were grouped according to their degree of mineralization and metal content, from the most depleted to the most metal-enriched, as serpentinites (Sp), stockwork serpentinites (Sw), and semimassive sulfide serpentinites (SMS) [*Marques et al*., 2007] (Figure 10). The composition of our serpentinites overlaps the fields of nonmineralized and, to a lesser extent, stockwork serpentinites (Sp and Sw, Figure 10). Overall, our samples are depleted in Cu and Zn compared to those analyzed by *Marques et al*. [2007], with the notable exception of M7-PL4-09. They represent the least mineralized and depleted end-member composition of the basement of the Rainbow hydrothermal field.

Loss on ignition (LOI; Table 1) of analyzed serpentinites ranges from 12 to 17 wt %. LOI greater than 13–14 wt % is indicative of the variable development of a late clay-rich alteration or carbonation in addition to an

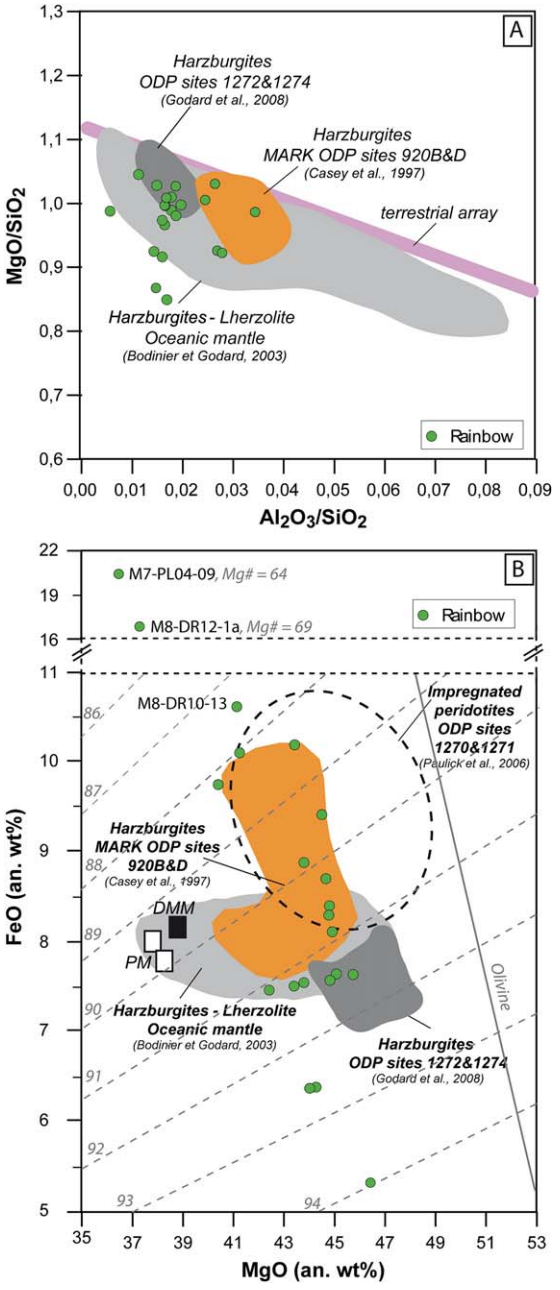

Figure 9. Bulk rock composition of the selected serpentinites collected in the Rainbow massif: (a) MgO/SiO_2 versus Al_2O_3/SiO_2, and (b) FeO_{Tot} versus MgO. Compositions are recalculated on a volatile-free basis (an. wt %). FeO_{Tot} stands for total FeO content. The terrestrial array on Figure 9a is from *Jagoutz et al.* [1979] and *Hart and Zindler* [1986]. In Figure 9b, dashed gray lines are iso-Mg# lines for Mg# = 100 × Mg/(Mg + Fe) cationic ratio while the thick gray line represents the stoichiometric variations of olivine Fe-Mg composition.

advanced serpentinization of peridotites (LOI ∼ 13 wt %). The highest contents in Ca (CaO = 1–4 wt %) correspond to serpentinites crosscut by Ca-carbonate veins. The high LOI values of samples showing relicts of primary minerals are explained by such late carbonate precipitates (e.g., M7-DR13-02). The Rainbow serpentinites have high degrees of bulk iron oxidation (Fe^{3+}/Fe_{Tot} = 0.43–0.82; Table 1), typical of highly (>60%) to fully serpentinized peridotites [*Evans*, 2008; *Andreani et al.*, 2013b]. Analyses of three variably serpentinized domains of sample M8-DR06-01 (M8-DR06-01a, M8-DR06-01b, and M8-DR06-01c; Table 1) testify to the progressive increase of iron oxidation state (from 0.43 to 0.57) during serpentinization. In contrast, the formation of the orange-brown alteration crust (e.g., sample M7-PL4-14) and the hydrothermal mineralization is not associated with significant modification of the serpentinite ferric iron content. The highest values of Fe^{3+}/Fe_{Tot} (>0.75) are associated with the formation of iron-rich, oxidative red veins or patches. The ferric iron content is not correlated to the total iron content of the rock.

4.4.2. Rare Earth Elements (REE)

Chondrite-normalized REE patterns of serpentinized peridotites are shown in Figure 11 together with the compositions of seawater, Rainbow vent fluids, and previously analyzed Rainbow serpentinites [*Douville et al.*, 2002; *Marques et al.*, 2007]. Our serpentinite samples have depleted and variable REE compositions compared to the previously published data for Rainbow. Europium anomalies (Eu/Eu*; Table 1) are also variable (0.2–16.6) and can be similar to or higher than that of seawater (0.6–1) and of Rainbow vent fluids (∼40).

Three types of REE patterns were identified (Table 1 and Figure 11):

Type 1 patterns represent the majority of the samples. They are U-shaped to flat, ranging from the most depleted to the most enriched samples. Type 1 serpentinites have positive Eu anomalies (1.5–16) and

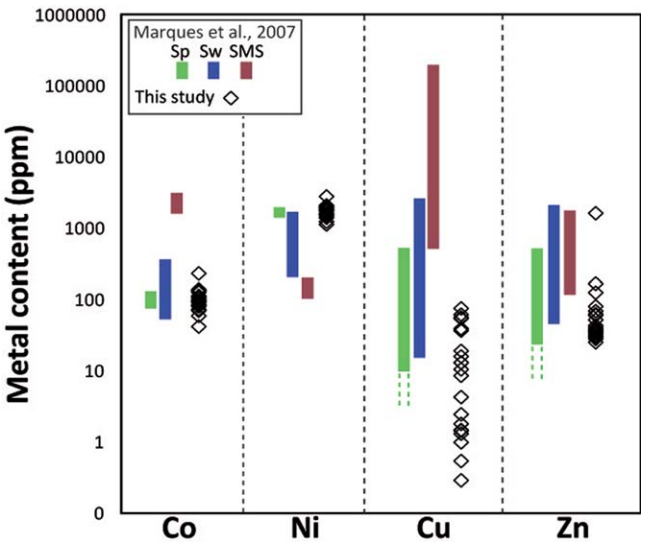

Figure 10. Metal content of the selected serpentinites collected throughout the Rainbow massif. They are compared to the metal content of other serpentinites (Serp), stockwork serpentinites (Sw), and semimassive sulfide samples (SMS) previously sampled within the active Rainbow field [*Marques et al.*, 2007].

display various degrees of LREE enrichment. These REE compositions are common in oceanic serpentinites and fall within the range of compositions of ultramafic rocks sampled along the Mid-Atlantic Ridge (e.g., ODP Leg 209 [*Paulick et al.*, 2006] and Atlantis Massif [*Boschi et al.*, 2006a; *Godard et al.*, 2009]). The most REE-enriched samples (M7-PL4-14a and M7-PL4-14b and M8-DR06-03) overlap in composition with the previously analyzed Rainbow serpentinites. The remaining serpentinites represent the most depleted samples observed at Rainbow; they have low Heavy REE (HREE) (Yb $\sim$ 0.1 $\times$ CI-chondrite) and Medium REE (MREE) contents (Gd $\sim$ 0.003–0.8 $\times$ CI-chondrite) and display selective enrichment in Light REEs (LREE) (La/Sm = 0.8–58 CI-chondrite). The Eu anomaly tends to increase with flattening of the pattern, except for samples M7-PL4–14a (orange-brown crust) and M8-DR12-1a (mineralized) which have a lower Eu anomaly for high LREE content. The two analyzed domains (a and b) of sample M7-PL4-14 indicate that the late orange-brown alteration (M7-PL4–14a = orange-brown crust) occurring over the Rainbow massif significantly increases all REE contents, and tends to reduce the Eu anomaly compared to green serpentinites (M7-PL4-14b). Mineralization seems to increase only LREE contents, as observed for sample M8-DR12-1a collected in the Rainbow stockwork, while its positive Eu anomaly remains significantly smaller than that of vent fluids. In contrast, the degree of serpentinization (M8-DR06-1 from domain c to a) progressively increases the Eu anomaly (1.5–3.3) and the MREE and LREE content.

Type 2 patterns are flat REE patterns with REE-normalized values ranging between 0.1 and 1, and no Eu anomalies. They are seen in four samples (M8-DR09-1a, M8-DR10-13, M8-DR12-4a, and M8-DR13-1a) coming from regions of strong hydrothermalism, i.e., around the Rainbow stockwork (M8-DR12 and DR13) and Clamstone (M8-DR09), and from the high-T outflow region of M8-DR10. They share mineralogical features of strong oxidative alteration, with iron-rich red coronas and veins, or yellow-green textures. These samples have high values of Fe^{3+}/Fe_{Tot} (>0.7) and are rich in Fe compared to Type 1 serpentinites (FeO_{Tot} = 8.3–9.1 wt %; Figure 9b). They are enriched in all incompatible immobile trace elements (Table 1) although none of them can be petrographically related to impregnation textures. These geochemical characteristics suggest that melt-rock reactions could have contributed to the enriched compositions of Type 2 serpentinites.

Type 3 patterns correspond to five samples that present a LREE enrichment with negative Eu anomalies (M7-PL4-05, M7-PL4-06, M7-PL4-09, M7-PL10-7, and M7-DR13-2). Serpentinite M7-PL4-09, the most mineralized sample of this study, is LREE-enriched (100 $\times$ CI-chondrite for La), similar to vent fluids and Rainbow SMS (Figure 11c) [*Marques et al.*, 2007], but it has a strong negative Eu anomaly, in contrast to vent fluids and previous data. The other samples display smaller negative Eu anomalies, closer to that of seawater. M7-PL4-05 and M7-PL10-7 present high FeO_{Tot} contents ($9 < FeO_{Tot} < 11$ wt %; Figure 9b) that fall within the field of impregnated peridotites, suggesting a possible effect of melt-rock reaction on the REE pattern. These five samples do not share any other petrographic or geochemical similarities.

4.4.3. Fluid Mobile Elements (FME)

Fluid mobile elements (FME) such as semivolatile elements (As, Sb), large ion lithophile elements (LILE: Rb, Sr, Cs, Ba, U) and light elements (Li) are considered to be good markers of fluid circulation and fluid-rock

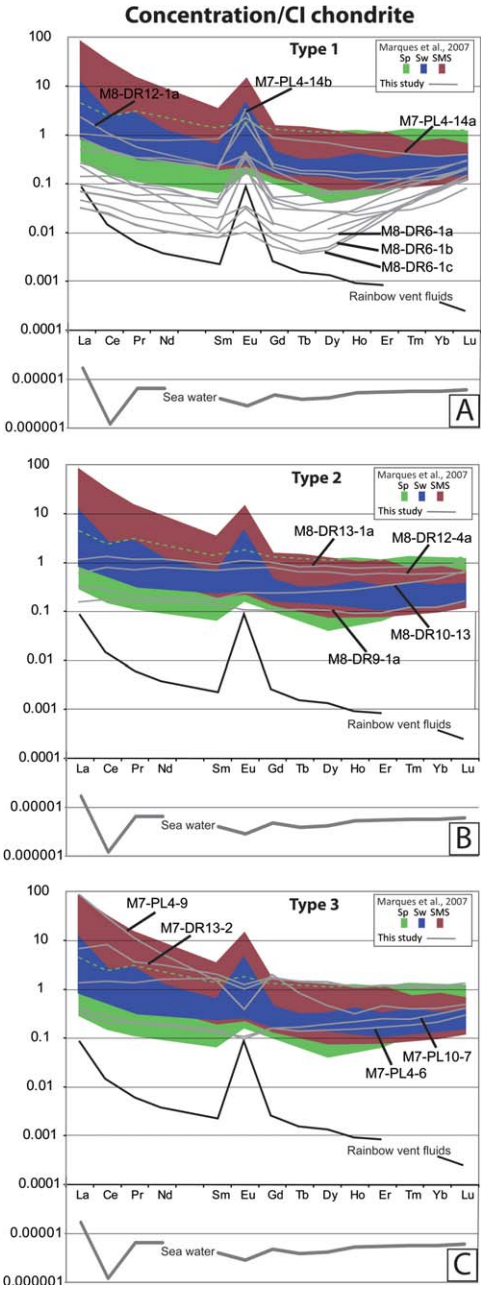

Figure 11. Rare earth element concentrations normalized to chondrite [*McDonough and Sun*, 1995] of selected serpentinites collected in the Rainbow massif. They are compared to the REE patterns of other serpentinites (Sp: green area limited by the green dotted line), of stockwork serpentinites (Sw), and of semimassive sulfide samples (SMS) previously sampled within the active Rainbow field [*Marques et al*., 2007]. Seawater and Rainbow fluid patterns are also shown for reference [*Douville et al*., 2002].

reactions. Serpentinites typically act as a trap for these elements during alteration of ultramafic rocks [e.g., *Deschamps et al*., 2011].

The Rainbow serpentinites have Li contents ranging from 0.04 to 2.2 ppm, typical of abyssal serpentinized peridotites (0.07–4 ppm) [*Vils et al*., 2008], with the exception of four Li-rich samples (7.3–14.8 ppm; Table 1). Li content appears little affected by the degree of serpentinization in our samples. It varies from 0.77 to 1.34 ppm for the increasingly serpentinized sample domains M8-DR6-1c to M8-DR6-1a. Similar enrichments in Li have been attributed to interaction with a fluid previously modified by basalts [*Decitre et al*., 2002].

The U content is variable in Rainbow serpentinites; it ranges between 0.3 and 1.1 ppm, except for the least serpentinized of the Rainbow samples, M8-DR6-1c (U = 0.001 ppm). U enrichment is typically attributed to late seafloor alteration [e.g., *Niu*, 2004; *Godard et al*., 2009].

Most samples have Ba contents ranging between ~0.1 and 1.4 ppm, which is close to the evolution range of the different domains of sample M8-DR6-1 with increasing degrees of serpentinization (0.2–2.4 ppm). Neither the degree of serpentinization, nor the formation of orange-brown or red alteration textures changes the Ba (and Rb) content. However, petrographic observations and the positive correlation between Ba content and Sr and Ca contents indicate that the distribution of these elements is controlled by the presence of Ca-carbonates in the sample. This is in agreement with the fact that Sr is not correlated to Eu/Eu*, suggesting that positive Sr and Eu anomalies are not due to the presence of trace amounts of plagioclase in the rock [e.g., *Godard et al*., 2009].

A linear correlation trend is observed between As and Sb (Figure 12). Rainbow serpentinites have compositions ranging from those of primitive mantle to those of abyssal sediments and mantle wedge serpentinites [*Hattori and Guillot*, 2003; *Plank and Ludden*, 1992]. End-members of this linear trend are seawater, similar to

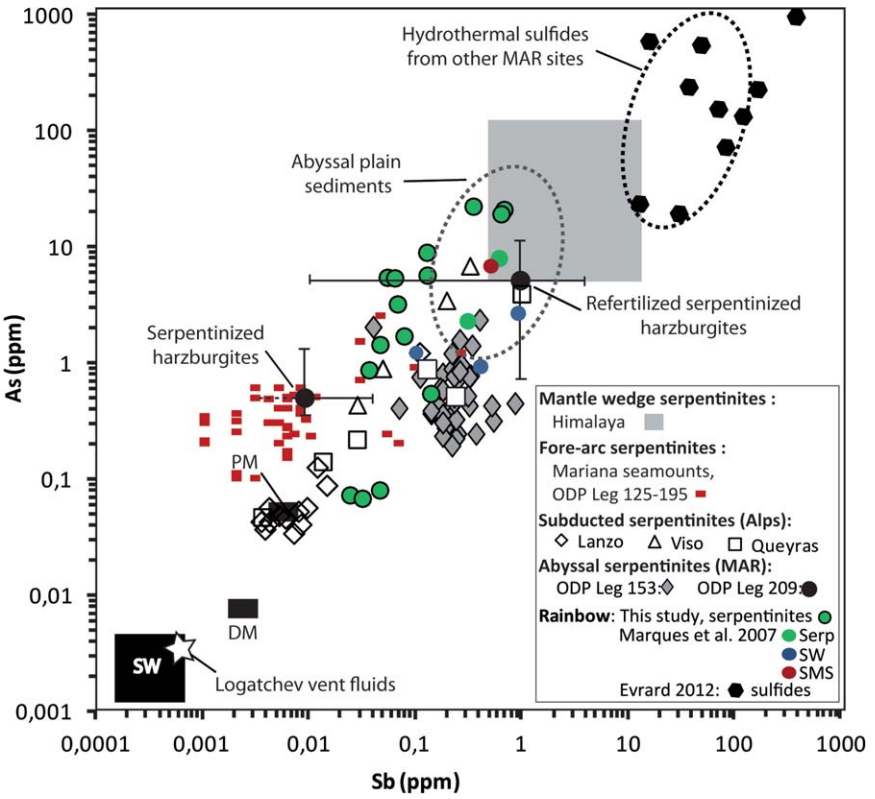

Figure 12. Plot of As versus Sb bulk concentrations of the selected Rainbow serpentinites, and bulk rock analyses of serpentinites from other geological settings. Mantle wedge serpentinites from *Hattori and Guillot* [2003]; fore-arc serpentinites from *Savov et al.* [2005, 2007]; subducted serpentinites from *Lafay et al.* [2013] and *Debret et al.* [2013]; abyssal serpentinites of ODP Leg 153 (23°21′N, MAR) from *Burgath* [1997] and *Werner and Pilot* [1997]; abyssal serpentinites of ODP Leg 209 (15°20′N, MAR) from *Paulick et al.* [2006]; hydrothermal sulfides from other MAR sites from *Evrard* [2012] and *Fouquet et al.* [2010]; abyssal plain sediments from *Plank and Ludden* [1992]; seawater (SW) and Logatchev vent fluids from *Douville et al.* [2002] and *Schmidt et al.* [2007]; composition of primitive mantle (PM) and depleted mantle (DM) from *McDonough and Sun* [1995] and *Salters and Stracke* [2004].

the hydrothermal fluid composition, and sulfide compositions from MAR hydrothermal fields. As and Sb values at Rainbow are more variable than those of other abyssal serpentinites or fore-arc serpentinites. As content (up to 22.6 ppm) also reaches high values (>>2 ppm), which have previously only been found in subduction zone serpentinites. The highest contents (~5–20 ppm) are observed in samples from the Clamstone (M8-DR9-1a), Ghost City (M8-DR11-6), and Rainbow hydrothermal sites (M7-PL4-5, M7-PL10-7, M8-DR12-4, M8-DR13-1a, and M7-DR13-2). Samples enriched in As and Sb also have the highest Pb, Cu, and Zn contents, with Pb up to 3 ppm, Cu ~40–78 ppm, and Zn ~60–170 ppm. Our observations suggest that these elements are hosted in sulfides precipitated within serpentinites in hydrothermal areas.

4.5. Stable Isotope Geochemistry of Serpentinites

The O and H isotopic compositions of 14 serpentinite samples are given in Table 1 and plotted in Figure 13. O isotope compositions of Rainbow serpentinites show a large range of values, from +0.64 to +5.10‰ (V-SMOW), within the range of oceanic serpentinites. They are lower than unaltered mantle values (+5.7 ± 0.2‰) [*Harmon and Hoefs*, 1995]. They show a linear trend from mantle values to seawater (0‰) and hydrothermal fluid (~1‰) [*Jean-Baptiste et al.*, 1997] values (Figure 13). Hydrogen isotope compositions range from −55 to −72‰ (V-SMOW; Table 1) and fall within the range of oceanic serpentinites (−85 to −30‰) [*Wenner and Taylor*, 1973; *Sheppard*, 1980; *Agrinier et al.*, 1988; *Sakai et al.*, 1990; *Agrinier et al.*, 1995, 1996]. These values are higher than the δD value previously reported for Rainbow hydrothermal fluids (−120‰) [*Jean-Baptiste et al.*, 1997] but lower than that of seawater (0‰) (Figure 13).

Serpentinization temperatures (Tables 1 and S4) were calculated based on serpentine and water fractionation, neglecting δ^{18}O values of magnetite because of the difficulty of separating serpentine and magnetite grains from our samples. We assumed that the δ^{18}O values of serpentine minerals are close to those of bulk

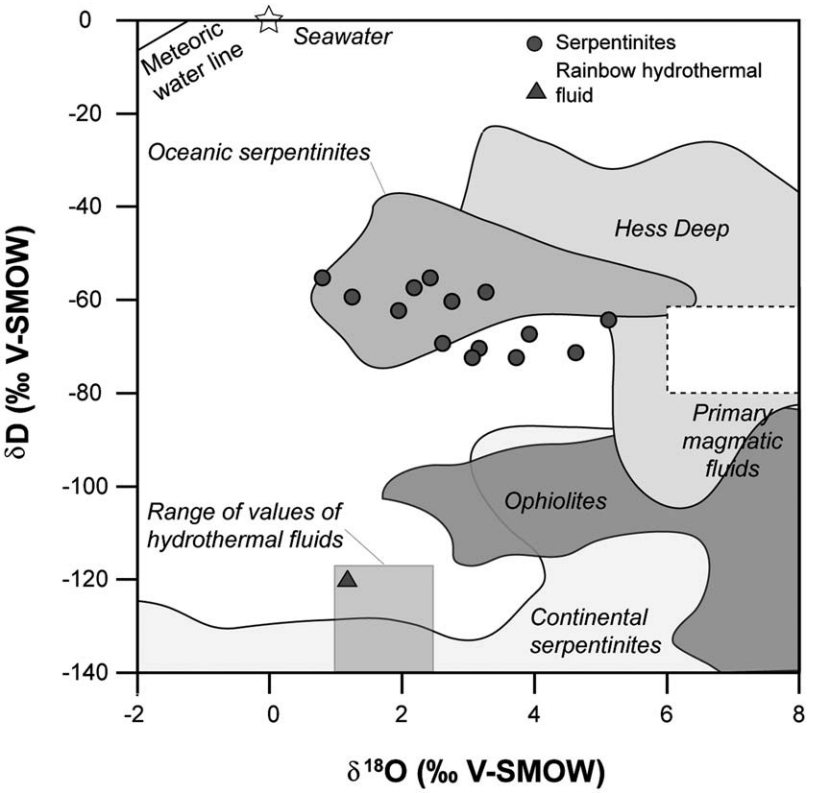

Figure 13. Oxygen and hydrogen isotopic compositions of the selected Rainbow serpentinites. δD values versus δ^{18}O values of serpentinites hosting the Rainbow hydrothermal system. The range of oceanic serpentinites is from *Wenner and Tayor* [1971] and *Agrinier et al.* [1995] for Hess Deep; while the ophiolite is from *Wenner and Taylor* [1974] and *Magaritz and Taylor* [1974]. Data on primary magmatic fluids are from *Stakes* [1991]. Oxygen isotope compositions of hydrothermal fluids are from *Jean-Baptiste et al*. [1997] and the range of δD values are for methane in hydrothermal fluids [*Proskurowski et al*., 2006].

rock serpentinites. The serpentinizing fluid is assumed to be seawater with a δ^{18}O value of 0‰ for most of the samples, except those previously identified as mineralized from petrographic and geochemical evidence. The latter, located near the active Rainbow site and in its stockwork (M7-PL4-9 and M8-DR12-1a), clearly underwent alteration by a high-T hydrothermal fluid, which is thus used for serpentinization T calculations (Table 1). For comparison, calculations with both fluids are presented for all samples in Table S4. However, the nature of the serpentinizing fluid is likely to be a mix between these two end-members, based on δD values.

Several thermometers [i.e., *Wenner and Taylor*, 1971; *Savin and Lee*, 1988; *Früh-Green et al*., 1996; *Zheng*, 1993; *Saccocia et al*., 2009], based on empirical, increment methods, or on experimental data, were used, and yield different temperatures (Table S4). Discrepancies between the different thermometers, likely related to the calibration method, provide a valuable temperature range which we simplified for discussion by averaging the four values (Tables 1 and S4). δ^{18}O values of the serpentinites indicate that temperatures are roughly comprised between 160 and 350°C on the Rainbow massif (Table 1). Sample M7-PL4–09 shows the highest temperatures of serpentinization (353°C), consistent with its location on the active Rainbow vent field, and with petrographic and geochemical evidence of mineralization (REE and metals; Table 1). The lowest temperature corresponds to a carbonated serpentinite (M8-DR9-1a) from the Clamstone site (166°C).

5. Discussion

5.1. Composition, Structure, and Tectonic History of the Rainbow Massif

The lithologies exposed on the Rainbow massif seafloor are consistent with the tectonic exhumation of deep-seated lower crust and upper mantle rocks, likely from a compositionally heterogeneous crust, as

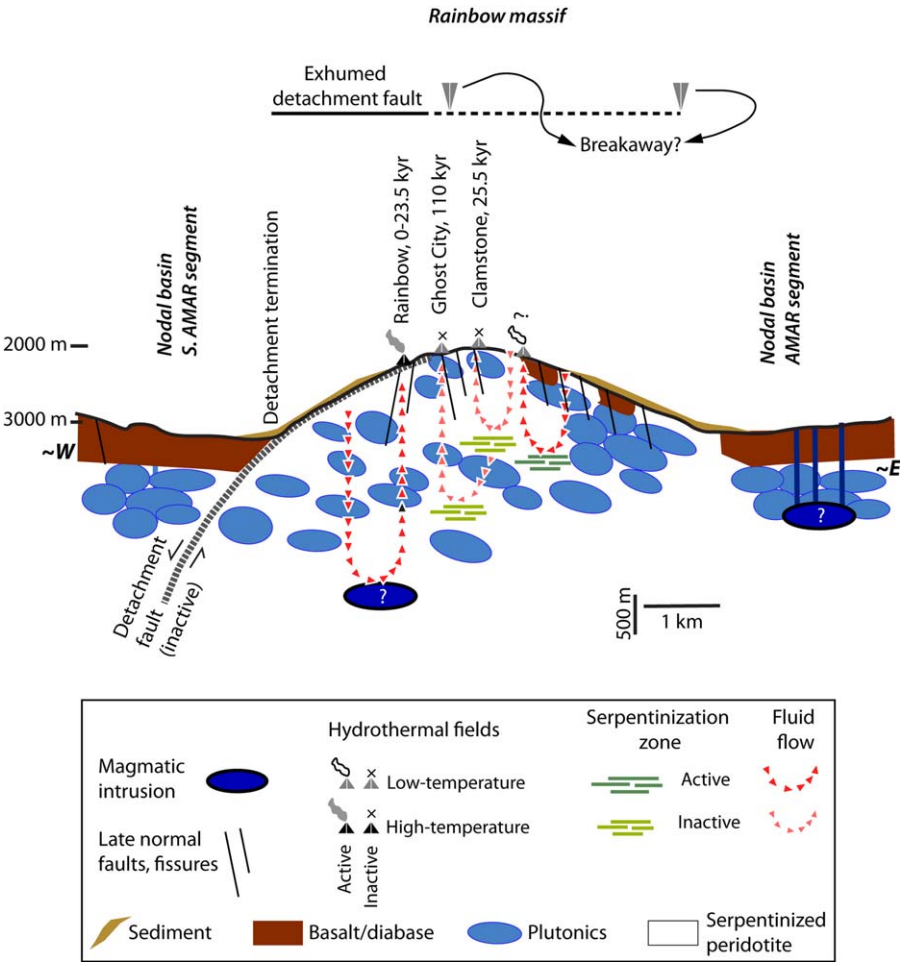

Figure 14. Schematic drawing of an E-W cross section of the Rainbow massif summarizing our proposed interpretation of the structural and hydrothermal observations.

observed in oceanic core complexes formed by detachment faulting elsewhere along slow and ultraslow spreading ridges. The massif corresponds to a local gravity high [e.g., *Thibaud et al*., 1998], indicative of a dynamically sustained topography, as described for oceanic core complexes [e.g., *Blackman et al*., 2009]. This gravity signature precludes a diapiric origin, as low-density material rising to the seafloor would either register no gravity anomaly or a negative one. In addition, most sampled rocks are weakly deformed or undeformed, and lack evidence of pervasive, high-strain plastic or brittle deformation which would be associated with highly sheared material from a diapiric extrusion.

We posit that uplift has been dominated by a west dipping, long-lived detachment fault (Figure 14). A first line of evidence for a detachment-origin of the massif is the clear curved termination between the west flank slope and the northern tip of the flat rift valley floor of the south AMAR segment. This geometry (Figure 1c) is reminiscent of terminations of inferred detachment geometry at depth observed in other oceanic detachments rooting at the axis elsewhere [e.g., *deMartin et al*., 2007; *MacLeod et al*., 2009; *Smith et al*., 2008]. A second line of evidence is related to the apparent lack of continuity between the Rainbow massif and the crust formed on the west flank of the AMAR segment to the north, separated by a bathymetrically low area. In contrast, to the south, the massif links with the first abyssal hill on the east flank of the S-AMAR segment.

Our data suggest that the east dipping basaltic layer reported by *Fouquet et al*. [1998] near Clamstone is not continuous (Figure 14), as serpentinized peridotites are exposed on the NE flank of the massif, near its intersection with the AMAR rift valley. This lithological distribution is not conclusive enough to identify a precise location for the detachment breakaway (Figure 14), but is consistent with a detachment fault developing

on the western flank of the massif, accommodating extension on the eastern flank of the S-AMAR segment. Later oblique faults dissecting the massif may have contributed to the exposure of peridotites on the NE flank of the massif, although the detailed tectonic setting in this area requires further in situ geological and geophysical data to be fully understood.

The widespread sediment cover, observed both in situ from deep-sea vehicles (start of M7-PL10 dive track) and inferred from dredges on the W and E flank, is responsible for the limited amount of rocks recovered from the western and eastern slopes, and may also explain the low abundance of fault rocks, which have only been recovered at three sites: M08-DR06, M08-DR12, and M08-DR15 (Figures 2 and 6). M08-DR12 and M08-DR15 are located on the western flank of the massif, within the stockwork region, while M08-DR06, located on the summit, is similar to detachment-related talc-amphibole-chlorite schists found elsewhere [*MacLeod et al*., 2002; *Escartín et al*., 2003; *Schroeder and John*, 2004; *Boschi et al*., 2006b].

The Rainbow massif detachment appears to be currently inactive. This is consistent with the relatively continuous sediment cover observed, particularly along the W flank of the massif, which would correspond to the most recently exhumed detachment fault. Recent deformation has been taken up by faults dissecting the massif that are oblique to spreading (Figure 1), consistent with available focal mechanisms in the area. These data point to a stress field with the least compressive stress rotated ~30° clockwise with respect to the plate separation direction (Figure 1). This is likely due to the transfer of stresses from the tips of the AMAR and S-AMAR segments, through a mechanically continuous NTO [e.g., *Fujita and Sleep*, 1978; *Grindlay and Fox*, 1993]. The development of this dense fault network crosscutting the footwall is inconsistent with an active detachment fault, which should act as a decoupling zone localizing deformation and concentrating seismicity as observed along other MAR detachments [e.g., *deMartin et al*., 2007; *Escartín et al*., 2008; *Grevemeyer et al*., 2013].

5.2. Water-Rock Reactions at the Rainbow Massif

Peridotites are the most abundant and widespread of all the primary lithologies sampled at the Rainbow massif, and are also the most altered. Petrographic observations indicate that peridotites record several stages of water-rock reactions starting with serpentinization, followed by (or associated with) variable degrees of carbonatization and oxidative alteration, and locally by high-T hydrothermal mineralization. No chronology could be observed between the last two events.

5.2.1. Background Hydrothermal Alteration of the Rainbow Massif Basement

The dominant hydrothermal alteration observed in Rainbow basement results from a widespread and pervasive fluid circulation associated with serpentinization of peridotites and, to a lesser extent, of the olivine-rich mafic units. The majority of serpentinized peridotites do not show the high-T mineralization and strong metal enrichment commonly associated with focused high-T hydrothermalism (Figure 10). These samples also record serpentinization temperatures of ~160–260°C in contrast to the mineralized samples that indicate T up to ~350°C. These basement serpentinites thus appear the best suited to study the background water-rock interactions in the Rainbow massif. This dominant, widespread serpentinization event is probably closely associated with lower T diffuse venting such as that inferred at Clamstone and Ghost City, considering their similarities with Lost City [*Lartaud et al*., 2011] where serpentinization T at depth is estimated at 200°C (±50°C) [*Allen and Seyfried*, 2004].

Rainbow serpentinites are dominated by the Type 1 REE pattern (LREE enrichment and positive Eu/Eu* anomalies; Figure 11) which differs from that of abyssal peridotites [*Niu*, 2004; *Bodinier and Godard*, 2013] but is very similar to that of Rainbow hydrothermal fluids. Hence, the dominant serpentinizing fluid is expected to have a REE pattern close to that of Rainbow high-T vent fluids (Figure 11). Our analyses show that this signature is progressively acquired during the widespread serpentinization phase. Therefore, the REE composition of the fluid responsible for both serpentinization and present-day high-T hydrothermalism is controlled by the same source, which is abundant and ubiquitous enough to control the fluid signature through time and space, despite extensive fluid-rock reactions.

Alteration of plagioclase at depth is generally proposed to explain the REE pattern of hydrothermal vent fluids such as those from Rainbow [*Klinkhammer et al*., 1994; *Douville et al*., 1999]. Indeed, plagioclase is particularly enriched in Eu and LREE compared to olivine and pyroxene, and these elements can be remobilized during water-gabbro reactions. Plagioclase is a main component of magmatic rocks; it is expected to be

abundant within the core complex-type Rainbow massif (Figure 2), and encountered by the fluid along its pathway through the massif. The reducing environment created by serpentinization together with the high Cl-content and low pH of the Rainbow fluids also favors the formation, at depth, of fluids enriched in LREE and with a positive Eu anomaly (high solubility of LREE and Eu^{2+}) [*Douville et al*., 1999]. This REE signature is then recorded by the initially LREE-depleted serpentinites at shallower levels when the physicochemical conditions change (e.g., mixing with seawater), decreasing the solubility of these elements. While the ionic ratios of Eu^{2+} and LREE are too large (similar to that of Ca^{2+}) to be stored within the serpentine mineral structure, other accessory phases or adsorbed complexes can host them. This is in agreement with the chemical study of Rainbow vent fluids by *Seyfried et al*. [2011], who propose a concomitant alteration of olivine and plagioclase at depth, thought to be more efficient than olivine alteration alone [*Andreani et al*., 2013a]. This may be related to the observed enhanced alteration of gabbros when in contact with peridotites (Figures 5e and 5f), in addition to the alteration of olivine-rich mafic units (Figure 5).

The orange-brown alteration product observed on some samples is enriched in LREE and shows a positive U anomaly. In these samples, the Eu anomaly is low and sometimes negative (Type 1; Figure 11). These compositions are consistent with low temperature, oxidizing, seafloor weathering, occurring near the surface where the fluid becomes dominated by seawater.

Local changes in REE distribution and concentration in the ascending fluid due to strong variations and gradients of physicochemical conditions in the host rock at shallow levels (e.g., T, pH, ligands availability, redox, and anhydrite precipitation) [*Sverjensky*, 1984; *Douville et al*., 1999] may be responsible for the wide range of REE patterns and Eu anomalies observed in serpentinites, in addition to the variability in fluid flux due to permeability heterogeneities. The possible effect of primary magmatic impregnation is difficult to address here, especially for serpentinites displaying a flat pattern (Type 2; Figure 11). However, primary melt-rock reactions are expected to modify the final absolute content of REE, especially LREE, without modifying the observed patterns due to advanced water-rock reaction.

5.2.2. High-T Versus Low-T Hydrothermal Activity at the Rainbow Massif: Geochemical Markers and Tectonic Control

The active Rainbow site is restricted to an area of ~200 m in diameter, although evidence of fluid outflow is found up to ~2.5 km away from the site. Past high-T hydrothermal activity at one other location (Figure 2) is demonstrated by the epidosite sample described above.

Mobility of metals during acidic, high-T fluid circulation is known to be very efficient, making metals good markers of high-T hydrothermalism. Cu, Co, and Zn enrichments in serpentinites from the Rainbow stockwork and vent field have been documented by *Marques et al*. [2007] and testify to the contribution of a mafic source at depth feeding present-day hydrothermal vent fluids. Serpentinization T in our two mineralized samples (305 and 408°C) are the highest values, with the most mineralized sample having the highest T. Examination of the metal distribution in our serpentinites at the massif scale reveals that significant metal enrichment is restricted to the region of the Rainbow active field but is not systematic in rocks collected within the Rainbow stockwork or active field. The same conclusion can be made for other locations where dive and petrographic observations indicate clearly high-T hydrothermal outflow (e.g., Figures 3a, 3b, and 3e; epidosite from dredge M8-DR10, Figures 4d). This suggests a strong localization of mineralization resulting from highly focused high-T outflow and resulting in chemical gradients, with heterogeneity down to at least the decimeter (sample) scale. Hence, the identification of the spatial distribution of past and present hydrothermal locations at the massif scale cannot rely solely on metal enrichments in rocks collected using dredging. Rock sampling in the active area shows that localized high-T hydrothermalism also tends to increase the LREE content of serpentinites without significantly changing the Eu/Eu* (Type 3 pattern). LREE concentrations increase by 1 or 2 orders of magnitude in mineralized samples, which is in agreement with previous data from *Marques et al*. [2007]. However, as for metals, this enrichment is only significant in mineralized samples. Elsewhere, it can be overwhelmed by serpentinization or seafloor alteration.

Past low-T diffuse hydrothermal outflow is documented at the Clamstone and Ghost City fossil hydrothermal sites. The serpentinization T calculated for samples collected at these sites indicate ~160 and 210°C, respectively. Sr isotope ratios of carbonates associated with the Ghost City fossil venting area are very similar to those of seawater [*Lartaud et al*., 2011] and confirm shallow water circulation in the footwall. FME measurement of serpentinites from these sites show amongst the highest enrichment in As (9–20 ppm).

Globally, Rainbow serpentinites fall within the range of values previously measured in abyssal serpentinites [*Deschamps et al*., 2013] for all FME except for As and Sb. A series of Rainbow serpentinites, with serpentinization T ranging between 160 and 220°C, shows the highest As concentrations reported in oceanic serpentinites (Figure 12), approaching that of subducted serpentinites from the Himalayas or Queyras, in which sediment contamination is invoked to explain such enrichment [*Hattori and Guillot*, 2003; *Lafay et al*., 2013]. *Hattori et al*. [2005] showed that most of the As in mantle wedge serpentinites is oxidized as As(V) and incorporated within the serpentine structure. Depending on its redox state, As can also integrate sulfides or overlay their altered surface, or be adsorbed onto the surface of silicates, oxides, oxi-hydroxides, or organic compounds [e.g., *Smedley and Kinniburgh*, 2002; *Takahashi et al*., 2004]. Here, the positive correlation between Pb, Cu(-Zn), and As(-Sb) suggests that hydrothermal mineralization played a role in the whole-rock enrichment that tends toward the hydrothermal sulfide composition (Figure 12). Hence, As(-Sb) enrichments are interpreted here as markers of lower T ($<$220°C) pervasive hydrothermal fluid circulation, which did not result in massive deposits, but precipitated micrometric sulfides and possibly enriched serpentine minerals in all these elements.

The location of both active and fossil hydrothermal sites suggests that fluid flow localizes along recent faults and fractures rather than along the inactive detachment. The Rainbow field is associated with a 25 m high fault scarp [*Fouquet et al*., 2010] at the intersection between NE-SW and N-S normal faults (Figures 1c and 1d). The low-T Clamstone Field extends along both the top and base of a ~20 m high normal fault scarp trending ~30°N (Figure 1d), which is part of the set of oblique faults visible in the sonar and multibeam bathymetry (Figure 1). A similar association of faults and hydrothermal outflow has been observed elsewhere, such as the basalt-hosted TAG and Lucky Strike hydrothermal fields [e.g., *Bohnenstiehl and Kleinrock*, 1999; *Barreyre et al*., 2012] along the MAR. These observations further confirm that normal faults act as preferential fluid discharge zones, with permeability likely increased by damage along, and in the vicinity of, the fault plane [*Hirose and Hayman*, 2008]. The lack of organized spatial distribution of the type or composition of hydrothermal fluids (they all have one dominant REE pattern), as inferred from rock composition in addition to fluid chemistry at the Rainbow site, suggests that fluid localization and associated compositional variability (in FME, Eu/Eu*, metals, T or redox) occurs at a smaller spatial scale than that of the sampling and observations available for the Rainbow massif (~2–4 km).

Dating of hydrothermal deposits from the three sites shows no clear spatiotemporal progression. The oldest hydrothermal deposits dated at the active Rainbow field yield a U/Th age of 23 $\pm$ 1.5 kyr [*Kuznetsov et al*., 2006], which is similar to the ^{14}C age of ~25 kyr reported for the low-T fossil Clamstone site [*Lartaud et al*., 2010]. The low-T fossil site of Ghost City yields U/Th ages that range from 46 $\pm$ 0.3 to 195 $\pm$ 11 kyr, with the most representative age at 110 $\pm$ 0.9 kyr. This age corresponds to the sample with a geochemical signature that is more consistent with seawater interaction [*Lartaud et al*., 2011]. These results suggest that Ghost City activity did not overlap with that of Rainbow and Clamstone. They also constrain the minimum age for the oblique fault network that must have formed prior to the oldest available hydrothermal date (~110 kyr). No dating is available for the high-T activity associated with the epidosite sample, although we do not preclude that, owing to its position on the massif and by analogy with ophiolites, it may relate to deep-seated hydrothermal activity prior to massif exhumation.

Figure 14 provides a conceptual model of the recent and present-day distribution of hydrothermal activity at the Rainbow massif, and its controlling processes. Both the locations and ages of the hydrothermal sites clearly suggest that all known hydrothermal activity was posterior to the detachment fault activity and the exhumation of the massif and that it is associated with the late, oblique fault system crosscutting the Rainbow massif. If we consider that the detachment breakaway corresponds to the summit of the massif, the horizontal fault displacement is ~4 km, which corresponds to ~0.4 Myr of fault slip assuming the present-day full spreading rate (~21 km/Myr) and symmetric spreading, or somewhat less (~0.25 Myr) if the detachment accommodated up to 70–80% of the plate separation, as observed elsewhere [e.g., *Baines et al*., 2008; *Grimes et al*., 2008]. Finally, the ages of the three hydrothermal sites do not show any systematic progression consistent with the age of the seafloor as inferred from both spreading rate and distance between sites along a flow line. This is consistent with ephemeral active sites (possibly operating for up to several tens of thousands years), distributed throughout the massif. We do not discard the possibility of presently active low-T hydrothermal activity (associated with serpentinization) at this massif, which would be diffuse and would produce clear fluids that cannot be easily detected in the water column, as observed in nearby NTO

massifs such as Saldanha [*Dias et al*., 2011]. Available field observations remain very limited (mainly the Rainbow and Clamstone sites, in addition to the two Nautile tracks), and most of the seafloor of the Rainbow massif has not been inspected yet (Figure 2).

The heat source at the origin of the active and fossil sites is not well constrained. Low-T hydrothermal activity, associated with metal-poor fluids (e.g., Clamstone and Ghost City sites), is likely associated with zones of active serpentinization at depth, with little or even no magmatic component, which are ultimately responsible for the pervasive alteration of peridotites throughout the massif. However, serpentinization reaction alone may not be able to drive hydrothermal circulation, as debated for the off-axis Lost City field [*Allen and Seyfried*, 2004]. For the Rainbow massif, its dating points to almost contemporaneous high-T (Rainbow) and low-T hydrothermal (Clamstone) activity at a distance of a few km. These two sites might have shared a common heat source in the past and testify to heterogeneous fluid circulation within the massif with localized discharge zones displaying a distinct character. The high-T Rainbow site is likely associated with a magmatic source at depth, although heat flux estimates may indicate heat extraction over a significant ridge length, if a steady state oceanic accretion is assumed [*German and Lin*, 2004]. This may be achieved by mining heat from the lithospheric mantle of the nearby ridge sections [*German et al*., 2010b], located ~6 and ~8 km east and west of the active site, which can provide the required heat to animate both the low-T and high-T hydrothermal circulations, simultaneously or otherwise. Alternatively, elevated heat fluxes may be transient, associated with localized magmatic bodies episodically emplaced, and cooled by hydrothermal activity (Figure 14).

6. Conclusions

Based on the interpretation of bathymetry, geophysical data, and geological observations from the Rainbow area, we propose that this and other massifs found along nontransform offsets of the Mid-Atlantic ridge are oceanic core complexes exhumed by oceanic detachment faults. In the case of Rainbow, the west dipping detachment fault is now inactive, and recent to present-day deformation is accommodated by a network of NW-SE normal faults that crosscut the massif. These late faults provide an extended network for fluid circulation, even away from a localized heat source and control the location of both the active vent site (Rainbow) and fossil hydrothermal fields (Clamstone and Ghost City) over the last 110 kyr, at least.

The dominant, background, water-rock reaction in the basement is a widespread serpentinization stage that affected the variously impregnated peridotites at a T ranging from ~160 to 260°C, and to a lesser extent, the olivine-rich mafic units especially where they are at contact with ultramafics. High-T hydrothermal activity (~350°C), associated with strong LREE enrichment and massive sulfur mineralization, is highly localized and only observed in some samples from the active Rainbow field area or from an area 5 km NW of it. More pervasive, lower T (<220°C) hydrothermal activity can be inferred at various other locations within the massif, thanks to anomalously high As, Sb, and Pb contents in serpentinites, similar to the activity at Clamstone and Ghost City. We infer that the fluids responsible for the serpentinization stage and the low-T hydrothermal activity are chemically similar to the ones actively venting at the Rainbow hydrothermal field and that they record reactions of the fluid with mafic-ultramafic rocks at depth. These results thus suggest that fluids circulating in the Rainbow massif should be compositionally stable through space and time, and over a T range of 160–350°C, since Clamstone and Rainbow were simultaneously active in the past. The late alteration stages locally modified the geochemical signature of serpentinites (REE and U contents) and include abundant carbonate precipitation at lower T and under more oxidizing conditions (weathering).

Inferences on the tectonic setting and fluid-rock reactions within the massif from observations made at Rainbow may also be extended to other NTO massifs where efficient fluid circulation may be maintained in the basement even after the cessation of detachment faulting. Our results also demonstrate the importance of pervasive diffuse outflow at the massif scale, and the marked heterogeneity of fluid circulation at the kilometer to meter scale, which may be attributable to the variability of fluid pathways as a result of the competing effects of magmatism, tectonic fracturing, and reaction clogging.

Acknowledgments
We thank E. Gracia for providing high-resolution TOBI imagery of the area and for discussions during the writing of this manuscript. Data and samples used in this study were obtained during the 2007 and 2008 MOMARDREAM cruises onboard N/O Pourquoi Pas? And N/O l'Atalante, financed by CNRS/IFREMER (France). We are grateful for the work of the Crew, Officers, Science Teams, and the operators of the deep-sea vehicles, and to the PI of the 2007, F. Gail. We also want to thank Nicolas Hayman and an anonymous reviewer from their constructive comments that considerably improved the manuscript. This is IPGP contribution 3556.

References

Agrinier, P., M. Javoy, and J. Girardeau (1988), Hydrothermal activity in a peculiar oceanic ridge: Oxygen and hydrogen isotope evidence in the Xigaze ophiolite (Tibet, China), *Chem. Geol.*, *71*, 313–335, doi:10.1016/0009-2541(88)90057-5.

Agrinier, P., R. Hékinian, D. Bideau, and M. Javoy (1995), O and H stable isotope compositions of oceanic crust and upper mantle rocks exposed in the Hess Deep near the Galapagos Triple Junction, *Earth Planet. Sci. Lett.*, *136*, 183–196.

Agrinier, P., G. Cornen, and M.-O. Beslier (1996), Mineralogical and oxygen isotopic features of serpentinites recovered from the ocean/continent transition in the Iberia Abyssal Plain, in *Proceedings of Ocean Drilling Program, Scientific Results*, vol. 149, edited by R. B. Whitmarsh et al., pp. 541–552, Ocean Drill. Program, College Station, Tex.

Allen, D. E., and W. E. Seyfried (2004), Serpentinization and heat generation: Constraints from Lost City and Rainbow hydrothermal systems, *Geochim. Cosmochim. Acta*, *68*, 1347–1354.

Andreani, M., I. Daniel, and M. Pollet-Villard (2013a), Aluminium speeds up the hydrothermal alteration of olivine, *Am. Mineral.*, *98*, 1738–1744.

Andreani, M., M. Muñoz, C. Marcaillou, and A. Delacour (2013b), μXANES study of iron redox state in serpentine during oceanic serpentinization, *Lithos*, *178*, 70–83.

Bach, W., N. R. Banerjee, H. J. B. Dick, and E. T. Baker (2002), Discovery of ancient and active hydrothermal systems along the ultra-slow spreading Southwest Indian Ridge 10°–16°E, *Geochem. Geophys. Geosyst.*, *3*(7), 1044, doi:10.1029/2001GC000279.

Baines, A. G., M. J. Cheadle, B. E. John, and J. J. Schwartz (2008), The rate of oceanic detachment faulting at Atlantis Bank, SW Indian Ridge, *Earth Planet. Sci. Lett.*, *273*, 105–114, doi:10.1016/j.epsl.2008.06.013.

Barreyre, T., J. Escartín, R. Garcia, M. Cannat, E. Mittelstaedt, and R. Prados (2012), Structure, temporal evolution, and heat flux estimates from the Lucky Strike deep-sea hydrothermal field derived from seafloor image mosaics, *Geochem. Geophys. Geosyst.*, *13*, Q04007, doi:10.1029/2011GC003990.

Barriga, F. J. A. S., I. M. A. Costa, J. M. R. Relvas, A. Ribeiro, Y. Fouquet, H. Ondréas, L. Parson, and FLORES Scientific Party (1997), The Rainbow serpentinites and serpentinite-sulfide stock work (Mid-Atlantic Ridge, AMAR segment): A preliminary report of the FLORES results, *Eos Trans. AGU*, *78*, 832.

Barriga, F. J. A. S., et al. (1998), Discovery of the Saldanha hydrothermal field on the Famous segment of the MAR (36°30′N), *Eos Trans. AGU*, *79*(45), Fall Meet. Suppl., F67.

Barriga, F. J. A. S., et al. (2003), SEAHMA-1 cruise report (July-August 2002), Creminer, Fac. of Sci. Univ. of Lisbon, Lisbon, Portugal.

Beltenev, V., et al. (2007), A new hydrothermal field at 13°30′N on the Mid-Atlantic Ridge, *InterRidge News*, *16*, 9–11.

Blackman, D. K., J.-P. Canales, and A. Harding (2009), Geophysical signatures of oceanic core complexes, *Geophys. J. Int.*, *178*, 593–613.

Bodinier, J.-L., and M. Godard (2013), Orogenic, ophiolitic, and abyssal peridotites, in *The Mantle and Core: Treatise on Geochemistry*, 2nd ed., edited by K. K. Turekian and H. D. Holland, Elsevier, Oxford, U. K.

Bogdanov, Y., A. Sagalevitch, E. Chernyaev, A. Ashadze, E. Gurvich, V. Lukashin, G. Ivanov, and V. Peresypkin (1995), A study of the hydrothermal field at 14°45′N on the Mid Atlantic Ridge using the MIR submersibles, *BRIDGE Newsl.*, *9*, 9–13.

Bohnenstiehl, D., and M. C. Kleinrock (1999), Faulting and fault scaling on the median valley floor of the Trans-Atlantic Geotraverse (TAG) segment, 26 N on the Mid-Atlantic Ridge, *J. Geophys. Res.*, *104*, 29,351–29,364.

Boschi, C., G. L. Früh-Green, A. Delacour, J. A. Karson, and D. S. Kelley (2006a), Mass transfer and fluid flow during detachment faulting and development of an oceanic core complex, Atlantis Massif (MAR 30°N), *Geochem. Geophys. Geosyst.*, *7*, Q01004, doi:10.1029/2005GC001074.

Boschi, C., G. L. Früh-Green, and J. Escartín (2006b), Occurrence and significance of serpentinite-hosted, talc-and amphibole-rich fault rocks in modern oceanic settings and ophiolite complexes: An overview, *Ofioliti*, *31*, 129–140.

Burgath, K.-P., V. Marchig, and K. Mussallam (1997), Data report: Mineralogic, structural, and chemical variability of mantle sections from Holes 920B and 920D, in *Proceedings of Ocean Drilling Program, Scientific Results*, vol. 153, edited by J. A. Karson et al., pp. 505–521, Ocean Drill. Program, College Station, Tex.

Charlou, J. L., J. P. Donval, E. Douville, J. Knoery, Y. Fouquet, H. Bougault, B. P. Jean, M. Stievenard, and C. R. German (1997), High methane flux between 15°N and the Azores triple junction, Mid-Atlantic Ridge; hydrothermal and serpentinization processes, *Eos Trans. AGU*, *78*(46), Fall Meet. Suppl., F831.

Charlou, J. L., J. P. Donval, Y. Fouquet, P. Jean-Baptiste, and N. Holm (2002), Geochemistry of high H_2 and CH_4 vent fluids issuing from ultramafic rocks at the Rainbow hydrothermal field (36°14′N, MAR), *Chem. Geol.*, *191*, 345–359.

Charlou, J. L., J. P. Donval, C. Konn, H. Ondreas, Y. Fouquet, P. Jean-Baptiste, and E. Fourre (2010), High production and fluxes of H_2 and CH_4 and evidence of abiotic hydrocarbon synthesis by serpentinization in ultramafic-hosted hydrothermal systems on the Mid-Atlantic Ridge, in *Diversity of Hydrothermal Systems on Slow Spreading Ocean Ridges, Geophys. Monogr. Ser.*, vol. 188, edited by P. A. Rona et al., pp. 321–367, AGU, Washington, D. C.

Debret, B., M. Andreani, M. Godard, C. Nicollet, S. Schwartz, and R. Lafay (2013), Trace element behavior during serpentinization/de-serpentinization of an eclogitized oceanic lithosphere: A LA-ICPMS study of the Lanzo ultramafic massif (Western Alps), *Chem. Geol.*, *357*, 117–133.

Decitre, S., E. Deloule, L. Reisberg, R. James, P. Agrinier, and C. Mével (2002), Behavior of Li and its isotopes during serpentinization of oceanic peridotites, *Geochem. Geophys. Geosyst.*, *3*(1), 1007, doi:10.1029/2001GC000178.

deMartin, B. J., R. A. Sohn, J. P. Canales, and S. E. Humphris (2007), Kinematics and geometry of active detachment faulting beneath the Trans-Atlantic Geotraverse (TAG) hydrothermal field on the Mid-Atlantic Ridge, *Geology*, *35*, 711, doi:10.1130/G23718A.1.

Deschamps, F., S. Guillot, M. Godard, M. Andreani, and K. Hattori (2011), Serpentinites act as sponges for fluid-mobile elements in abyssal and subduction zone environments, *Terra Nova*, *23*, 171–178.

Deschamps, F., M. Godard, S. Guillot, and K. Hattori (2013), Geochemistry of subduction zone serpentinites: A review, *Lithos*, *178*, 96–127.

Dias, A. S., G. L. Früh-Green, S. M. Bernasconi, and F. Barriga (2011), Geochemistry and stable isotope constraints on high-T activity from sediment cores of the Saldanha hydrothermal field, *Mar. Geol.*, *279*, 128–140, doi:10.1016/j.margeo.2010.10.017.

Douville, E., P. Bienvenu, J.-L. Charlou, J.-P. Donval, Y. Fouquet, P. Appriou, and T. Gamo (1999), Yttrium and rare earth elements in fluids from various deep-sea hydrothermal systems, *Geochim. Cosmochim. Acta*, *63*, 627–643.

Douville, E., J. J. Charlou, E. H. Oelkers, P. Bienvenu, C. F. J. Colon, J. P. Donval, Y. Fouquet, D. Prieur, and P. Appriou (2002), The Rainbow vent fluids (36°14′N, MAR): The influence of ultramafic rocks and phase separation on trace metal content in Mid-Atlantic Ridge hydrothermal fluids, *Chem. Geol.*, *184*, 37–48.

Dyment, J., K. Tamaki, H. Horen, Y. Fouquet, K. Nakase, M. Yamamoto, M. Ravilly, and M. Kitazawa (2005), A positive magnetic anomaly at Rainbow hydrothermal site in ultramafic environment, *Eos Trans. AGU*, *86*(52), Fall Meet. Suppl., OS21C-08.

Emmanuel, S., and B. Berkowitz (2006), Suppression and stimulation of seafloor hydrothermal convection by exothermic mineral hydration, *Earth Planet. Sci. Lett.*, *243*, 657–668.

Escartín, J., C. Mével, C. J. MacLeod, and A. M. McCaig (2003), Constraints on deformation conditions and the origin of oceanic detachments: The Mid-Atlantic Ridge core complex at 15°45′N, *Geochem. Geophys. Geosyst.*, *4*(8), 1067, doi:10.1029/2002GC000472.

Escartín, J., D. K. Smith, J. Cann, H. Schouten, C. H. Langmuir, and S. Escrig (2008), Central role of detachment faults in accretion of slow-spreading oceanic lithosphere, *Nature*, *455*, 790–794.

Evans, B. W. (2008), Control of the products of serpentinization by the Fe2+Mg-1 exchange potential of olivine and orthopyroxene, *J. Petrol.*, *49*, 1873–1887.

Evrard, C. (2012), Processus métallogéniques associés aux interactions hydrothermales entre l'eau de mer et les roches ultrabasiques du manteau le long de la ride Médio-Atlantique, PhD thesis, Univ. Bretagne Occidentale, Brest, France.

Fouquet, Y., and IRIS Scientific Party (2001), IRIS cruise report, IFREMER, Plouzane, France.

Fouquet, Y., et al. (1997), Discovery and first submersible investigations on the Rainbow hydrothermal field on the MAR (36°14N), *Eos Trans. AGU*, *78*(46), Fall Meet. Suppl., F832.

Fouquet, Y., et al. (1998), FLORES diving cruise with Nautile near the Azores—First dives on the Rainbow field: Hydrothermal seawater/mantle interaction, *InterRidge News*, *7*(1), 24–28.

Fouquet, Y., et al. (2010), Geodiversity of hydrothermal process along the Mid-Atlantic Ridge and ultramafic–hosted mineralization: A new type of oceanic Cu-Zn-Co-Au volcanogenic massive sulfide deposit, in Diversity of Hydrothermal Systems on Slow Spreading Ocean Ridges, Geophys. Monogr. Ser., vol. 188, edited by P. Rona et al., pp. 321–367, AGU, Washington, D. C.

Früh-Green, G. L., A. Plas, and C. Lécuyer (1996), Petrologic and stable isotope constraints on hydrothermal alteration and serpentinization of the EPR shallow mantle at Hess Deep (Site 895), in *Proceedings of Ocean Drilling Program, Scientific Results*, vol. 147, edited by C. Mével et al., pp. 255–291, Ocean Drill. Program, College Station, Tex.

Fujita, K., and N. H. Sleep (1978), Membrane stresses near mid-ocean ridge-transform intersections, *Tectonophysics*, *50*, 207–221.

German, C. R., and J. Lin (2004), The thermal structure of the oceanic crust, ridge-spreading and hydrothermal circulation: How well do we understand their inter-connections, in *Mid-Ocean Ridges: Hydrothermal Interactions Between the Lithosphere and Oceans, Geophys. Monogr. Ser.*, vol. 148, edited by C. R. German, J. Lin, and L. M. Parson, pp. 1–18, AGU, Washington, D. C.

German, C. R., et al. (1996), Hydrothermal exploration near the Azores Triple Junction: Tectonic control of venting at slow-spreading ridges?, *Earth Planet. Sci. Lett.*, *138*, 93–104.

German, C. R., E. T. Backer, C. Mevel, K. Tamaki, and The FUJI Science Team (1998), Hydrothermal activity along the southwest Indian ridge, *Nature*, *395*, 490–493.

German, C. R., et al. (2010a), Diverse styles of submarine venting on the ultraslow spreading Mid-Cayman Rise, *Proc. Natl. Acad. Sci. U. S. A.*, *107*, 14,020–14,025.

German, C. R., A. M. Thurnherr, J. Knoery, J. L. Charlou, P. J. Baptiste, and H. N. Edmonds (2010b), Heat, volume and chemical fluxes from submarine venting: A synthesis of results from the Rainbow hydrothermal field, 361N MAR, *Deep Sea Res., Part I*, *57*, 518–527.

Godard, M., Y. Lagabrielle, O. Alard, and J. Harvey (2008), Geochemistry of the highly depleted peridotites drilled at ODP Sites 1272 and 1274 (Fifteen-Twenty Fracture Zone, Mid-Atlantic Ridge): Implications for mantle dynamics beneath a slow spreading ridge, *Earth Planet. Sci. Lett.*, *267*, 410–425.

Godard, M., et al. (2009), Geochemistry of a long in-situ section of intrusive slow-spread oceanic lithosphere: Results from IODP Site U1309 (Atlantis Massif, 30°N Mid-Atlantic-Ridge), *Earth Planet. Sci. Lett.*, *279*, 110–122.

Gracia, E., L. M. Parson, D. Bideau, and R. Hekinian (1998), Volcano-tectonic variability along segments of the Mid-Atlantic Ridge between Azores platform and Hayes fracture zone: Evidence from submersible and high-resolution sidescan sonar data, *Geol. Soc. Spec. Publ.*, *148*, 1–15, doi:10.1144/GSL.SP.1998.148.01.01.

Gracia, E., J. L. Charlou, J. R. Radford-Knoery, and L. M. Parson (2000), Non-transform offsets along the Mid-Atlantic Ridge south of the Azores (38°N-34°N): Ultramafic exposures and hosting of hydrothermal vents, *Earth Planet. Sci. Lett.*, *177*, 89–103.

Grevemeyer, I., T. J. Reston, and S. Moeller (2013), Microseismicity of the Mid-Atlantic Ridge at 7°S-8°15′S and at the Logatchev Massif oceanic core complex at 14°40′N-14°50′N, *Geochem. Geophys. Geosyst.*, *14*, 3532–3554, doi:10.1002/ggge.20197.

Grimes, C. B., B. E. John, M. J. Cheadle, and J. L. Wooden (2008), Protracted construction of gabbroic crust at a slow spreading ridge: Constraints from 206Pb/238U zircon ages from Atlantis Massif and IODP Hole U1309D (30°N, MAR), *Geochem. Geophys. Geosyst.*, *9*, Q08012, doi:10.1029/2008GC002063.

Grindlay, N. R., and P. J. Fox (1993), Lithospheric stresses associated with non-transform offsets of the Mid-Atlantic Ridge: Implications for a finite element analysis, *Tectonics*, *12*, 982–1003.

Harmon, R. S., and J. Hoefs (1995), Oxygen isotope heterogeneity of the mantle deduced from global 18O systematics of basalts from different geotectonic settings, *Contrib. Mineral. Petrol.*, *120*, 95–114, doi:10.1007/BF00311010.

Hart, S. R., and A. Zindler (1986), In search of a bulk-Earth composition, *Chem. Geol.*, *57*, 247–267, doi:10.1016/0009–2541(86)90053-7.

Hattori, K., and S. Guillot (2003), Volcanic fronts form as a consequence of serpentinite dehydration in the forearc mantle wedge, *Geology*, *31*, 525–528.

Hattori, K., Y. Takahashi, S. Guillot, and B. Johanson (2005), Occurrence of arsenic (V) in forearc mantle serpentinites based on X-ray absorption spectroscopy study, *Geochim. Cosmochim. Acta*, *69*, 5585–5596.

Hirose, T., and N. W. Hayman (2008), Structure, permeability, and strength of a fault zone in the footwall of an oceanic core complex, the Central Dome of the Atlantis Massif, Mid-Atlantic Ridge, 30°N, *J. Struct. Geol.*, *30*, 1060–1071.

Jagoutz, E., H. Palme, and H. Baddenhausen (1979), The abundances of major, minor and trace elements in the earth's mantle as derived from primitive ultramafic nodules, *Lunar Planet. Sci.*, *2*, 2031–2050.

Jean-Baptiste, P., J. L. Charlou, and M. Stievenard (1997), Oxygen isotope study of mid-ocean ridge hydrothermal fluids: Implications for the oxygen-18 budget of the oceans, *Geochim. Cosmochim. Acta*, *61*, 2669–2677.

Kelley, D. S., et al. (2001), An off-axis hydrothermal vent field near the Mid-Atlantic Ridge at 30 degrees N, *Nature*, *412*, 145–149.

Kelley, D. S., et al. (2005), A serpentinite-hosted ecosystem: The Lost City hydrothermal field, *Science*, *307*, 1428–1434.

Klinkhammer, G. P., H. Elderfield, J. M. Edmond, and A. Mitra (1994), Geochemical implications of rare earth element patterns in hydrothermal fluids from mid-ocean ridges, *Geochim. Cosmochim. Acta*, *58*, 5105–5113.

Konn, C., J.-L. Charlou, J.-P. Donval, N. G. Holm, F. Dehairs, and S. Bouillon (2009), Hydrocarbons and oxidized organic compounds in hydrothermal fluids from Rainbow and Lost City ultramafic-hosted vents, *Chem. Geol.*, *258*, 299–314.

Kumagai, H., et al. (2008), Geological background of the Kairei and Edmond hydrothermal fields along the Central Indian Ridge: Implications of their vent fluids' distinct chemistry, *Geofluids*, *8*, 239–251.

Kuznetsov, V. Y. U., G. A. Cherkashev, A. Y. Lein, V. Shilov, F. Maksimov, K. Arslanov, T. Stepanova, N. Baranova, S. Chernov, and D. Tarasenko (2006), 230Th/U dating of massive sulfides from the Logatchev and Rainbow hydrothermal fields (Mid-Atlantic Ridge), *Geochronometria*, *25*, 51–55.

Lafay, R., F. Deschamps, S. Schwartz, S. Guillot, M. Godard, and C. Nicollet (2013), High-pressure serpentinites, a trap-and-release system controlled by metamorphic conditions: Example from the Piedmont zone of the western Alps, *Chem. Geol.*, *343*, 38–54, doi:10.1016/j.chemgeo.2013.1002.1008.

Lartaud, F., et al. (2010), Fossil clams from a serpentinite-hosted sedimented vent field near the active smoker complex Rainbow, MAR, 36°13′N: Insight into the biogeography of vent fauna, *Geochem. Geophys. Geosyst.*, *11*, Q0AE01, doi:10.1029/2010GC003079.

Lartaud, F., C. T. S. Little, M. De Rafelis, G. Bayon, J. Dyment, B. Ildefonse, Y. Fouquet, F. Gaill, and N. Le Bris (2011), Fossil evidence for serpentinization fluids fueling chemosynthetic assemblages, *Proc. Natl. Acad. Sci. U. S. A.*, *108*, 7968–7703, doi:10.1073/pnas.1009383108.

Le Douaran, S., H. D. Needham, and J. Francheteau (1982), Pattern of opening rates along the axis of the Mid-Atlantic Ridge, *Nature*, *300*, 254–257.

Lowell, R. P., and P. A. Rona (2002), Seafloor hydrothermal systems driven by the serpentinization of peridotite, *Geophys. Res. Lett.*, *29*(11), 1531, doi:10.1029/2001GL014411.

MacLeod, C. J., J. Escartín, D. Banerji, G. J. Banks, M. Gleeson, D. H. B. Irving, R. M. Lilly, A. M. McCaig, Y. Niu, and S. Allerton (2002), Direct geological evidence for oceanic detachment faulting: The Mid-Atlantic Ridge, 15 45′N, *Geology*, *30*, 879–882.

MacLeod, C. J., R. C. Searle, B. J. Murton, J. F. Casey, C. Mallows, S. C. Unsworth, K. L. Achenbach, and M. Harris (2009), Life cycle of oceanic core complexes, *Earth Planet. Sci. Lett.*, *287*, 333–344, doi:10.1016/j.epsl.2009.08.016.

Magaritz, M., and H. P. Taylor Jr. (1974), Oxygen and hydrogen isotope studies of serpentinization in the Troodos ophiolite Complex, Cyprus, *Earth Planet. Sci. Lett.*, *23*, 8–14.

Marques, A. F. A., F. Barriga, V. Chavagnac, and Y. Fouquet (2006), Mineralogy, geochemistry, and Nd isotope composition of the Rainbow hydrothermal field, Mid-Atlantic Ridge, *Miner. Deposita*, *41*, 52–67, doi:10.1007/s00126-005-0040-8.

Marques, A. F. A., F. J. A. S. Barriga, and S. D. Scott (2007), Sulfide mineralization in an ultramafic-rock hosted seafloor hydrothermal system: From serpentinization to the formation of Cu–Zn–(Co)-rich massive sulfides, *Mar. Geol.*, *245*, 20–39.

McCaig, A. M., A. Delacour, A. E. Fallick, T. Castelain, and G. L. Früh-Green (2010), Detachment fault control on hydrothermal circulation systems: Interpreting the subsurface beneath the TAG hydrothermal field using the isotopic and geological evolution of oceanic core complexes in the Atlantic, in Diversity of Hydrothermal Systems on Slow Spreading Ridges, Geophys. Monogr. Ser., vol. 188, edited by P. A. Rona et al., AGU, Washington, D. C.

McDonough, W. F., and S. S. Sun (1995), The composition of the Earth, *Chem. Geol.*, *120*, 223–253.

Melchert, B., et al. (2008), First evidence for high-T off-axis venting of deep crustal/mantle heat: The Nibelungen hydrothermal field, southern Mid-Atlantic Ridge, *Earth Planet. Sci. Lett.*, *275*, 61–69.

Niu, Y. (2004), Bulk-rock major and trace element compositions of abyssal peridotites: Implications for mantle melting, melt extraction and post-melting processes beneath mid-ocean ridges, *J. Petrol.*, *45*, 2423–2458.

Ohara, Y., et al. (2012), A serpentinite-hosted ecosystem in the Southern Mariana Forearc, *Proc. Natl. Acad. Sci. U. S. A.*, *109*, 2831–2835.

Ondréas, H., M. Cannat, Y. Fouquet, and A. Normand (2012), Geological context and vents morphology of the ultramafic-hosted Ashadze hydrothermal areas (Mid-Atlantic Ridge 13°N), *Geochem. Geophys. Geosyst.*, *13*, Q0AG14, doi:10.1029/2012GC004433.

Paulick, H., W. Bach, M. Godard, J. C. M. De Hoog, G. Suhr, and J. Harvey (2006), Geochemistry of abyssal peridotites (Mid-Atlantic Ridge, 15°20′N, ODP Leg 209): Implications for fluid/rock interaction in slow spreading environments, *Chem. Geol.*, *234*, 179–210.

Pedersen, R. B., I. H. Thorseth, T. E. Nygård, M. Lilley, and D. S. Kelley (2010), Hydrothermal activity at the Arctic Mid-Ocean Ridges, in Diversity of Hydrothermal Systems on Slow Spreading Ocean Ridges, Geophys. Monogr. Ser., vol. 188, edited by P. Rona et al., pp. 67–89, AGU, Washington, D. C.

Plank, T., and J. N. Ludden (1992), Geochemistry of sediments in the Argo Abyssal Plain at Site 765: A continental margin reference section for sediment recycling in subduction zones, in *Proceedings of Ocean Drilling Program, Scientific Results*, vol. 123, edited by F. M. Gradstein et al., pp. 167–189, Ocean Drill. Program, College Station, Tex.

Proskurowski, G., M. D. Lilley, D. S. Kelley, and E. J. Olson (2006), Low temperature volatile production at the Lost City hydrothermal field, evidence from a hydrogen stable isotope geothermometer, *Chem. Geol.*, *229*, 331–343.

Saccocia, P. J., J. S. Seewald, and W. C. Shanks (2009), Oxygen and hydrogen isotope fractionation in serpentine–water and talc–water systems from 250 to 450°C, 50MPa, *Geochim. Cosmochim. Acta*, *73*, 6789–6804.

Sakai, R., M. Kusakabe, M. Noto, T. Ishii (1990), Origin of waters responsible for serpentinization of the Izu-Ogasawara-Mariana forearc seamounts in view of hydrogen and oxygen isotope ratio, *Earth and Planet. Sci. Lett. 100*, 291–303.

Salters, V., and A. Stracke (2004), Composition of the depleted mantle, *Geochem. Geophys. Geosyst.*, *5*, Q05B07, doi:10.1029/2003GC000597.

Savin, S. M., and M. L. Lee (1988), Isotopic studies of phyllosilicates, *Rev. Mineral.*, *19*, 189–223.

Savov, I. P., J. G. Ryan, M. D'Antonio, K. Kelley, and P. Mattie (2005), Geochemistry of serpentinized peridotites from the Mariana Forearc Conical Seamount, ODP Leg 125: Implications for the elemental recycling at subduction zones, *Geochem. Geophys. Geosyst.*, *6*, Q04J15, doi:10.1029/2004GC000777.

Savov, I. P., J. G. Ryan, M. D'Antonio, and P. Fryer (2007), Shallow slab fluid release across and along the Mariana arc-basin system: Insights from geochemistry of serpentinized peridotites from the Mariana fore arc, *J. Geophys. Res.*, *112*, B09205, doi:10.1029/2006JB004749.

Schmidt, K., A. Koschinsky, D. Garbeschonberg, L. Decarvalho, and R. Seifert (2007), Geochemistry of hydrothermal fluids from the ultramafic-hosted Logatchev hydrothermal field, 15°N on the Mid-Atlantic Ridge: Temporal and spatial investigation, *Chem. Geol.*, *242*, 1–21.

Schroeder, T., and B. E. John (2004), Strain localization on an oceanic detachment fault system, Atlantis Massif, 30°N, Mid-Atlantic Ridge, *Geochem. Geophys. Geosyst.*, *5*, Q11007, doi:10.1029/2004GC000728.

Seyfried, W. E., N. J. Pester, K. Ding, and M. Rough (2011), Vent fluid chemistry of the Rainbow hydrothermal system (36°N, MAR): Phase equilibria and in situ pH controls on subseafloor alteration processes, *Geochim. Cosmochim. Acta*, *75*, 1574–1593.

Sheppard, S. M. (1980), Isotopic evidence for the origins of water during metamorphic processes in oceanic crust and ophiolitic complexes, *Colloq. Int. C. N. R. S.*, *272*, 135–147.

Sloan, H., and P. Patriat (1992), Kinematics of the North American-African plate boundary between 28° and 29°N during 10 Ma: Evolution of the axial geometry and spreading rate and direction, *Earth Planet. Sci. Lett.*, *113*, 323–341.

Smedley, P. L., and D. G. Kinniburgh (2002), A review of the source, behaviour and distribution of arsenic in natural waters, *Appl. Geochem.*, *17*, 517–568.

Smith, D. K., and J. R. Cann (1990), Hundreds of small volcanoes on the median valley floor of the Mid-Atlantic Ridge, *Nature*, *344*, 427–431.

Smith, D. K., M. Tolstoy, C. G. Fox, D. R. Bohnenstiehl, H. Matsumoto, and M. Fowler (2002), Hydroacoustic monitoring of seismicity at the slow-spreading Mid-Atlantic Ridge, *Geophys. Res. Lett.*, *29*(11), 1518, doi:10.1029/2001GL013912.

Smith, D. K., J. Escartín, M. Cannat, M. Tolstoy, C. G. Fox, D. Bohnenstiehl, and S. Bazin (2003), Spatial and temporal distribution of seismicity along the northern Mid-Atlantic Ridge (15°-35°N), *J. Geophys. Res.*, *108*(B3), 2167, doi:10.1029/2002JB001964.

Smith, D. K., J. Escartín, H. Schouten, and J. R. Cann (2008), Fault rotation and core complex formation: Significant processes in seafloor formation at slow-spreading mid-ocean ridges (Mid-Atlantic Ridge, 13°-15°N), *Geochem. Geophys. Geosyst.*, *9*, Q03003, doi:10.1029/2007GC001699.

Stakes, D. S. (1991), Oxygen and hydrogen isotope compositions of oceanic plutonic rocks: High-T deformation and metamorphism of oceanic layer 3, *Spec. Publ. Geochem. Soc.*, *3*, 77–90.

Sverjensky, D. A. (1984), Europium redox equilibria in aqueous solution, *Earth Planet. Sci. Lett.*, *67*, 70–78.

Takahashi, Y., R. Minamikawa, K. H. Hattori, K. Kurishima, N. Nihou, and K. Yuita (2004), Arsenic behaviour in paddy fields during the cycle of flooded and non-flooded periods, *Environ. Sci. Technol.*, *38*, 1038–1044.

Thibaud, R., P. Gente, and M. Maia (1998), A systematic analysis of the Mid-Atlantic Ridge morphology between 15°N and 40°N: Constraints of the thermal structure, *J. Geophys. Res.*, *103*, 24,233–24,243.

Tivey, M., and J. Dyment (2010), The magnetic signature of hydrothermal systems in slow spreading environments, in *Diversity of Hydrothermal Systems on Slow Spreading Ocean Ridges, Geophys. Monogr. Ser.*, vol. 188, edited by P. Rona et al., pp. 43–66, AGU, Washington, D. C.

Tivey, M. A., and H. P. Johnson (2002), Crustal magnetization reveals subsurface structure of Juan de Fuca Ridge hydrothermal vent fields, *Geology*, *30*, 979–982.

Tivey, M. A., P. A. Rona, and H. Schouten (1993), Reduced crustal magnetization beneath the active sulfide mound, TAG hydrothermal field, Mid-Atlantic Ridge, at 26°N, *Earth Planet. Sci. Lett.*, *115*, 101–115.

Tucholke, B. E., S. E. Humphris, and H. J. B. Dick (2013), Cemented mounds and hydrothermal sediments on the detachment surface at Kane Megamullion: A new manifestation of hydrothermal venting, *Geochem. Geophys. Geosyst.*, *14*, 3352–3378, doi:10.1002/ggge.20186.

Vils, F., L. Pelletier, A. Kalt, O. Müntener, and T. Ludwig (2008), The lithium, boron and beryllium content of serpentinized peridotites from ODP Leg 209 (Sites 1272A and 1274A): Implications for lithium and boron budgets of oceanic lithosphere, *Geochim. Cosmochim. Acta*, *72*, 5475–5504.

Wenner, D. B., and H. P. Taylor Jr. (1971), Temperatures of serpentinization of ultramafic rocks based on $^{18}O/^{16}O$ fractionation between coexisting serpentine and magnetite, *Contrib. Mineral. Petrol.*, *32*, 165–185.

Wenner, D. B., and H. P. Taylor, Jr. (1973), Oxygen and hydrogen isotope studies of the serpentinization of ultramafic rocks in oceanic environments and continental ophiolite complexes, *Am. J. Sci.*, *272*, 207–239.

Wenner, D. B., and H. P. Taylor Jr. (1974), $^{18}O/^{16}O$ and D/H studies of serpentinization of ultramafic rocks, *Geochim. Cosmochim. Acta*, *38*, 1255–1286.

Werner, C.-D., and J. Pilot (1997), Data report: Geochemistry and mineral chemistry of ultramafic rocks from the Kane area (MARK), in *Proceedings of Ocean Drilling Program, Scientific Results*, vol. 153, edited by J. A. Karson et al., pp. 457–470, Ocean Drill. Program, College Station, Tex.